

QUASI-TWO-DIMENSIONALITY OF THREE-DIMENSIONAL, MAGNETICALLY DOMINATED, DECAYING TURBULENCE

SHREYA DWIVEDI^{1,2,†}, CHANDRANATHAN ANANDAVIJAYAN^{1,*}, AND PALLAVI BHAT^{1,‡}

¹International Centre for Theoretical Sciences, Tata Institute of Fundamental Research, Bangalore 560089, India and

²Department of Physics, University of Wisconsin-Madison, Madison, WI 53706, USA

Version September 9, 2024

ABSTRACT

Decaying magnetohydrodynamic (MHD) turbulence is important in various astrophysical contexts, including early universe magnetic fields, star formation, turbulence in galaxy clusters, magnetospheres and solar corona. Previously known in the nonhelical case of magnetically dominated decaying turbulence, we show that magnetic reconnection is important also in the fully helical case and is likely the agent responsible for the inverse transfer of energy. Again, in the fully helical case, we find that there is a similarity in power law decay exponents in both 2.5D and 3D simulations. To understand this intriguing similarity, we investigate the possible quasi-two-dimensionalization of the 3D system. We perform Minkowski functional analysis and find that the characteristic length scales of a typical magnetic structure in the system are widely different, suggesting the existence of local anisotropies. Finally, we provide a quasi-two-dimensional hierarchical merger model which recovers the relevant power law scalings. In the nonhelical case, we show that a helicity-based invariant cannot constrain the system, and the best candidate is still anastrophy or vector potential squared, which is consistent with the quasi-two-dimensionalization of the system.

Subject headings: plasmas – magnetic fields – magnetohydrodynamics(MHD) – turbulence – magnetic reconnection

1. INTRODUCTION

Astrophysical plasmas are typically in a state of turbulence. In the aftermath of energetic processes that are responsible for generation of the turbulence, the plasma undergoes relaxation, leading to the decay of velocity and magnetic fields. Many astrophysical plasmas such as solar and stellar coronae, accretion disks, and pulsar magnetospheres host magnetic fields of significant strength and are magnetically dominated (Pevtsov et al. 2003; Blandford et al. 2017; Narayan et al. 2003). Such magnetic turbulent systems are thought to relax via magnetic reconnection (Taylor 1986). Reconnection is a process by which magnetic fields undergo topological reconfiguration accompanied by conversion of magnetic energy into heat, radiation and particle acceleration. These can be highly energetic events and are thought to explain solar flares, magnetospheric substorms, gamma-ray bursts etc (Ruan et al. 2020; Hesse & Cassak 2020; McKinney & Uzdensky 2012).

More recently, it was shown that magnetic reconnection plays an important role in 3D MHD decaying turbulence (Bhat et al. 2021; Zhou et al. 2020) further extending support to the idea of reconnection playing an important role in relaxation. Some of the astrophysical scenarios are either theoretically modelled or already well understood to relax via magnetic reconnections. For example, in the Sun, magnetic fields in the form of flux ropes extending up into the corona experience twists due to the motion of the foot points in the photosphere. The Parker model of coronal heating directly employs magnetic reconnection to relax such twisted magnetic flux ropes (Parker 1983). Inevitably, the nonlinear evolution of reconnecting flux ropes leads to turbulence (Rappazzo et al. 2008), accompanied by growth in magnetic structure size (Pontin et al. 2011). Another context is the interaction between solar

wind and earth’s magnetotail, which leads to reconnection. This involves magnetic flux loading and subsequent release of energy resulting in magnetospheric substorms (McPherron 1979). Thereafter, the earth’s magnetic field relaxes to its ground state, and these processes again feature turbulence (Daughton et al. 2011). In pulsar wind nebulae, the striped wind and large magnetic hoops are thought to relax via reconnections in decaying turbulence, leading to nonthermal emission and flares (Zrake 2016; Zrake & Arons 2017). Additionally, the magnetic dissipation due to post-shock instabilities seems to explain the lower strength of the magnetic field from observations (Porth et al. 2014).

Magnetic reconnection, as a model for relaxation, can also naturally explain the phenomenon of inverse energy transfer. Inverse energy transfer occurs when energy is transferred to larger scales as the turbulent system relaxes. In the 3D hydrodynamic case, relaxation of homogeneous and isotropic turbulence occurs by selective decay, i.e. energy at the smallest scales decays first, followed by decay of successively larger scales. This process does not lead to any inverse energy transfer but depicts what is known as the “permanence of large eddies” (Batchelor & Taylor 1949; Landau & Lifshitz 1975; Lesieur & Ossia 2000). On the other hand, it is well known that decaying 2D hydrodynamic turbulence can depict inverse energy transfer because here a different version of selective decay manifests. Here, one ideal invariant (kinetic energy) decays more slowly than another (enstrophy). In fact, the slower decay invariably is due to its condensation at larger scales, thus being consistent with the original understanding of selective decay (Matthaeus & Montgomery 1980; Ting et al. 1986). While permanence of large eddies just constitutes the continuation of the flow at larger scales (or smaller wavenumbers that are a part of the forward slope) at similar amplitudes, in other cases like 2D hydrodynamics or 3D MHD with magnetic helicity, the slower decaying ideal invariant can cause an

† sdwivedi4@wisc.edu

* chandranathan.a@icts.res.in

‡ pallavi.bhat@icts.res.in

actual inverse transfer in energy (involving increase of energy at larger scales or smaller wavenumbers) (Mininni & Pouquet 2013).

In the MHD case, it is easy to observe that in a 2D decaying system, an inverse transfer emerges as a consequence of reconnection between magnetic islands (Zhou et al. 2019). A similar process in 3D could lead to larger and larger magnetic structures at the cost of loss/decay in magnetic energy. The study in Bhat et al. (2021) (BZL21) shed light on the possibility of magnetic reconnection driving such a 3D inverse energy transfer. BZL21 were motivated by the observation that the decay laws in 3D simulations matched with that seen in 2D. They identified the dynamical timescale in this system of nonhelical decaying turbulence as the reconnection timescale, τ_{rec} . They found that the evolution curves collapsed when the time was normalized by the reconnection timescale. This result rules out the conventional notion that the dynamical time scale in a magnetically dominated system is typically the Alfvénic time scale. Thus, the inverse transfer phenomenon was shown to occur on a slower time scale.

The inverse transfer phenomenon is useful in astrophysical scenarios where the coherence length scale of the magnetic field is important as well. The ISM magnetic fields that first feed onto a central massive object need to be sufficiently coherent to trigger magnetorotational instability needed for angular momentum transport in accretion disks (Bhat et al. 2017). In galaxy clusters, large Faraday rotation measures need coherent magnetic fields (Subramanian et al. 2006; Bhat & Subramanian 2013). In IGM, the non-detection of GeV photons that should have originated from cascading of TeV photons emanating from blazars again needs coherent magnetic fields for deflecting charged particles (Neronov & Vovk 2010; Subramanian 2016; Hosking & Schekochihin 2023). The magnetic fields in ISM, galaxy clusters and IGM, as mentioned in the examples above, could have benefited from an inverse transfer in magnetic energy during a turbulent decaying phase (when the dynamo was inactive).

Direct numerical simulations of magnetically dominated turbulence have shown evidence for inverse energy transfer even when an ideally conserved quantity like magnetic helicity was absent (Brandenburg et al. 2015; Zrake 2014). BZL21 postulated that anastrophy conservation (in the absence of magnetic helicity) is responsible for the inverse transfer phenomenon in 3D. They highlighted the link between anastrophy conservation in the large Lundquist number limit and magnetic reconnection in 2D and claimed that this carries over to the case of 3D as well, thus explaining the exact similarity in the decay law between 2D and 3D. However, Hosking & Schekochihin (2021) introduced a new integral they call the Saffman helicity invariant based on magnetic helicity fluctuations, which they claimed is responsible for constraining the decay law (this does not give t^{-1} , but gives $t^{-1.18}$ instead). They extended the BZL21 result of τ_{rec} (reconnection timescale) being the dynamical timescale to the helical case as well and found that it leads to a $t^{-4/7}$ decay law.

In our work here, we examine helical decaying MHD turbulence and find that, indeed, reconnection is important in this case as well. It makes sense that reconnection is a common explanation for the phenomenon of structures growing larger and larger as the decay progresses in both helical and nonhelical inverse energy transfer. Intriguingly, the 2D(2.5D)-3D correspondence holds in the helical case as well; the decay law in 2.5D (magnetic helicity cannot be defined in the strict

2D case) is the same as that seen in 3D. We also assess the so-called Saffman helicity integral critically and find that it is most likely ruled out given the 2D-3D correspondence.

To assess the quasi-two-dimensional nature of the magnetically dominated decaying turbulence, we analyse the system using Minkowski functionals. These were originally introduced as a tool to study spatial patterns in galaxy cluster data (Mecke et al. 1994). In cosmology, it is well-known that there is clustering of galaxies (Peebles 1980). It was found that the two-point correlation function for large-scale galaxy clustering is insufficient due to non-gaussianity. Minkowski functionals, on the other hand, contain information related to all the correlation functions of the order and above two-point correlation (Wiegand et al. 2014). In this paper, we use these Minkowski functionals to examine the morphology of reconnecting fields and the associated current density structures. This tool was first used in this manner of assessing shapes in a scalar field in the field of cosmology and structure formation (Sahni et al. 1998). It has also been previously used in the field of astrophysical fluid dynamics for analysing magnetic field structures in simulations of small-scale dynamo (Wilkin et al. 2007; Seta et al. 2020). And to assess current density structures in strong MHD turbulence (Zhdankin et al. 2014). We primarily employ Minkowski functionals to quantify the inherent anisotropy within the system. This approach aids in refining our comprehension of the quasi-two-dimensional manifestation of the reconnections.

The following section covers the MHD equations, initial conditions and parameters employed in our direct numerical simulations. Section 3 delves into the analysis of data and results, with subsection 3.1 dedicated to the helical case and subsection 3.2 focusing on the nonhelical case. Within these subsections, we present evidence supporting the 2D-3D similarity in decay laws. Subsequent analyses compare conserved quantities and critically evaluate various integrals believed to constrain the evolution of these decaying systems. Section 4 presents results from the Minkowski functional analysis, followed by the introduction of an analytical quasi-2D hierarchical merger model in Section 5. The concluding sections, 6 and 7, consist of discussions and overall conclusions respectively. In the Appendix Sections A and B, we delineate the algorithms employed for Minkowski functional analysis.

2. NUMERICAL SETUP

2.1. The model

We have run direct numerical simulations of decaying helical and nonhelical MHD turbulence in 2.5D and 3D cubes, using PENCIL-CODE¹, with periodic boundary conditions. We solve the continuity equation, momentum equation and the uncoupled version of induction equations on a Cartesian N^2 or N^3 grid, where N is the number of grid points in any direction.

$$\frac{D \ln \rho}{Dt} = -\nabla \cdot \mathbf{u}, \quad (1)$$

$$\frac{D\mathbf{u}}{Dt} = -c_s^2 \nabla \ln \rho + \frac{\mathbf{J} \times \mathbf{B}}{\rho} + \frac{\mathbf{F}_{visc}}{\rho}, \quad (2)$$

$$\frac{\partial \mathbf{A}}{\partial t} = \mathbf{u} \times \mathbf{B} - \eta \mu_0 \mathbf{J}, \quad (3)$$

where $D/Dt = \partial/\partial t + \mathbf{u} \cdot \nabla$ is the advective derivative, \mathbf{u} is the fluid velocity field, $\mathbf{B} = \nabla \times \mathbf{A}$ is the magnetic field,

¹ <http://pencil-code.nordita.org>

Helicity	Resolution	$\eta \times 10^{-4}$	$\nu \times 10^{-4}$	u_{rms0}	B_{rms0}	$S/10^3$
nonhel	1024 ²	1.3	1.3	0.	0.4	0.8
nonhel	2048 ²	0.34	0.34	0.	0.4	3.
nonhel	4096 ²	0.168	0.168	0.	0.4	6.
hel	1024 ²	1.3	1.3	0.	0.4	0.8
hel	2048 ²	0.34	0.34	0.	0.4	3.
hel	4096 ²	0.168	0.168	0.	0.4	6.
nonhel	512 ³	5.4	5.4	0.	0.4	0.2
nonhel	1024 ³	2.5	2.5	0.	0.4	0.4
nonhel	1024 ³	1.3	1.3	0.	0.4	0.8
hel	512 ³	5.4	5.4	0.	0.4	0.2
hel	1024 ³	2.5	2.5	0.	0.4	0.4
hel	1024 ³	1.3	1.3	0.	0.4	0.8

TABLE 1: A summary of all the runs is listed. Helicity refers to whether the initial random magnetic field is fully helical (given by 'hel') or nonhelical (given by 'nonhel').

with \mathbf{A} the magnetic vector potential, and $\mathbf{J} = \nabla \times \mathbf{B}/\mu_0$ is the current density, with μ_0 the vacuum permeability, ρ is the mass density, and η is the magnetic diffusivity. The scalar potential $\Phi = 0$ (Weyl gauge), and the viscous force $\mathbf{F}_{visc} = \nabla \cdot 2\nu\rho\mathbf{S}$, where ν is the kinematic viscosity, and \mathbf{S} is traceless rate of strain tensor with components $S_{ij} = \frac{1}{2}(u_{i,j} + u_{j,i}) - \frac{1}{3}\delta_{ij}\nabla \cdot \mathbf{u}$ (commas denote partial derivatives).

A 2.5 simulation is similar to 2D, except the evolving characteristic field vectors have all three components along x , y and z . For instance, $\mathbf{B} = \nabla \times \mathbf{A}(x, y) = [B_x(x, y), B_y(x, y), B_z(x, y)]$.

While the system is isothermal with adiabatic index $\gamma = 1$, the variables ν , η and mean ρ remain constant throughout the decaying turbulence. All the quantities obtained from a simulation are dimensionless, characterized by length, velocity, density, and magnetic field, measured in the following units: system size (L), isothermal sound speed (c_s), initial density (ρ_0), and $\sqrt{\mu_0\rho_0c_s^2}$ respectively. Here, $L = 2\pi$ and $\rho_0 = \mu_0 = c_s = 1$.

2.2. Initial conditions and parameters

We initialize the magnetic vector potential component along j in the Fourier domain as follows,

Nonhelical magnetic case:

$$\hat{A}_j(\mathbf{k}) = h_j(\mathbf{k})(k/k_{cf})^{n/2-1} \quad (4)$$

Helical magnetic case:

$$\hat{A}_j(\mathbf{k}) = \left[\mathbf{P}_{jl} - i\sigma_M \epsilon_{jlm} \frac{k_m}{k} \right] h_j(\mathbf{k})(k/k_{cf})^{n/2-1} \quad (5)$$

where $j \in \{x, y, z\}$, $\mathbf{P}_{jl} = \delta_{jl} - k_j k_l / k^2$ is the projection operator, $\sigma_M = 1$ is the relative magnetic helicity, inducing fully helical magnetic field at $t = 0$, and

$$h_j(\mathbf{k}) = A_0 \exp(i\phi(\mathbf{k})) \exp\left(-\frac{1}{2} \frac{k^2}{k_{cf}^2}\right) \quad (6)$$

is a spectrum with amplitude A_0 , random phases $\phi(\mathbf{k})$ (between $-\pi$ to π) and Gaussian distributed fluctuations that exponentially cuts off beyond k_{cf} . This generates the shell integrated 1D magnetic power spectrum $M(k)$ that grows with a slope k^α , where the exponent $\alpha = 4$, and peaks at

$k_p \sim \frac{1}{L_{int}} \simeq 25$, over small scales at $t = 0$, where L_{int} is the integral length scale calculated as,

$$L_{int} = \frac{\int (2\pi/k)M(k)dk}{\int M(k)dk}, \quad (7)$$

and the initial root mean squared magnetic field $B_{rms0} = [2 \int M(k, t = 0)dk]^{1/2} \simeq 0.4$, the initial velocity field $u_{rms0} = 0$, and the magnetic Prandtl number = 1 for all the helical and nonhelical runs referred to in this paper.

The Lundquist number $S = (2\pi k_p^{-1})\sqrt{2E_M}/\eta$, where E_M is total magnetic energy. The initial parameters and configuration of the numerical simulations run on 1024², 2048² and 4096² grids in 2.5D, and 512³ and 1024³ grids in 3D, with high S , are shown in Table 1.

With the evolution of time, $M(k, t)$ decays with a slope of $k^{-5/2}$ for the helical magnetic decaying turbulence², whereas with a slope of k^{-2} for the nonhelical case (shown in a previous paper by Bhat et al. (2021) (BZL21).

3. RESULTS

3.1. Reconnection in helical decaying MHD turbulence

It has been well known that in a decaying turbulent system, if the magnetic fields are helical, then they tend to relax to larger scales. This results in an inverse cascade of magnetic helicity accompanied by a simultaneous inverse transfer of magnetic energy (Pouquet et al. 1976). The physical picture typically discussed involves twists or writhes in the field, relaxing to larger scales over a period of time. In this context, motivated by our previous results in BZL21, we explore if magnetic reconnection has a role to play in helical decaying MHD turbulence as well.

In Figs. 1 and 2, we show results from both 2.5D and 3D simulations. These were initialized with zero velocity field³ and random fully helical magnetic fields peaked at small scales which then decays as the simulations progress. In particular, we show the evolution curves of the rms value of the helical part of the magnetic field, defined as,

$$B_{rms}^H = \sqrt{2E_M^H}, \quad E_M^H = \frac{1}{2} \int kH(k)dk, \quad (8)$$

where $H(k)$ is the shell-averaged 1D spectrum of the magnetic helicity. In both the plots for 2.5D and 3D cases in Figs. 1 and 2, the difference between the top and bottom panels is that in the latter, the time axis is normalized by the magnetic reconnection time-scale $\tau_{rec} = S^{1/2}\tau_A$, where $\tau_A = (2\pi k_p^{-1})/\sqrt{2E_M}$ is the Alfvén time-scale. We observe that the B_{rms}^H evolution curves from runs with different Lundquist numbers collapse on top of each other. This reveals that the relevant dynamical time-scale is indeed the reconnection time-scale. This kind of collapse was first seen in Figs. 10 and 11 in BZL21, in the nonhelical decaying MHD turbulence case. Although the collapse in 3D is not as smooth as that in the 2.5D case, it can be inferred that the curves would asymptotically collapse at significantly higher Lundquist numbers. MHD simulations in 3D at Lundquist numbers larger than 800, i.e. at resolutions higher than 1024³, could not be conducted because of HPC resource constraints. The collapsing curves form the first part of the evidence for reconnection playing a

² refer Fig. 21 for power spectrum at different time snapshots

³ refer to Fig. 20 in the Appendix to view zero initial velocity field.

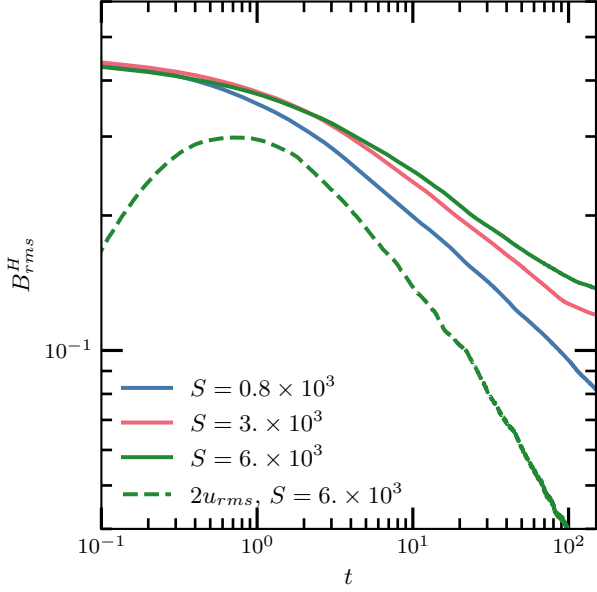


FIG. 1.—: Upper panel: evolution curves for B_{rms}^H and u_{rms} vs t from fully helical 2.5D runs with different values for S . Lower panel: collapse of the B_{rms}^H evolution curves when plotted against t/τ_{rec} .

role in decaying helical MHD turbulence. Next we study the slope of the decay curve.

One can calculate how the magnetic energy scales with time using simple considerations of power law decay (this is a standard method in hydrodynamics to derive decay scalings (Kolmogorov 1941)),

$$\frac{dE_M}{dt} \sim -\frac{E_M}{\tau_{rec}} \quad (9)$$

and the conservation of magnetic helicity, $\int \mathbf{A} \cdot \mathbf{B} dV$. Typically, the system under consideration is initialized to have a

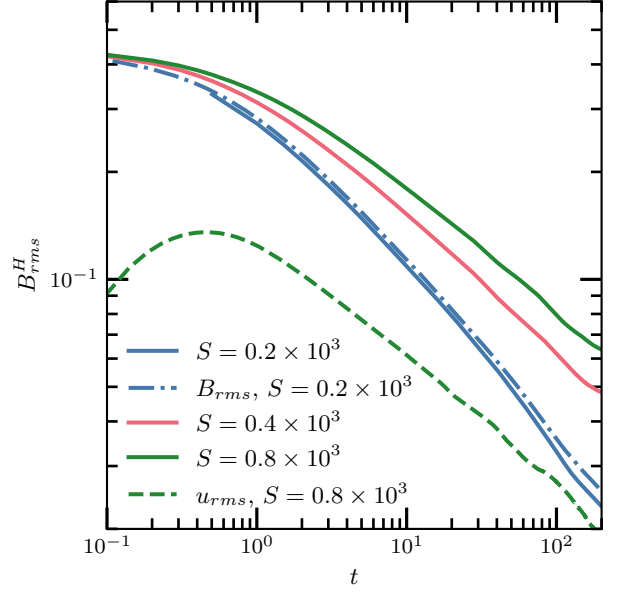


FIG. 2.—: Upper panel: evolution curves for B_{rms}^H and u_{rms} vs t from fully helical 3D runs with different values for S . Lower panel: collapse of the B_{rms}^H evolution curves when plotted against t/τ_{rec} .

spectrum that rises as k^4 , peaks at large wavenumbers, and falls quickly. Such a system, as it decays, retains this type of spectral shape with the peak shifting to the smaller wavenumbers. This indicates that the system, at any given time, has statistically more structures pertaining to the integral length scale or scales close to that corresponding to the peak wavenumber, k_p . This allows us to simplify and approximate our mathematical descriptions to follow the dynamics of the fields concentrated at k_p . With this in mind, one can simplify the conservation of magnetic helicity as,

$$E_M k_p^{-1} \sim const. \quad (10)$$

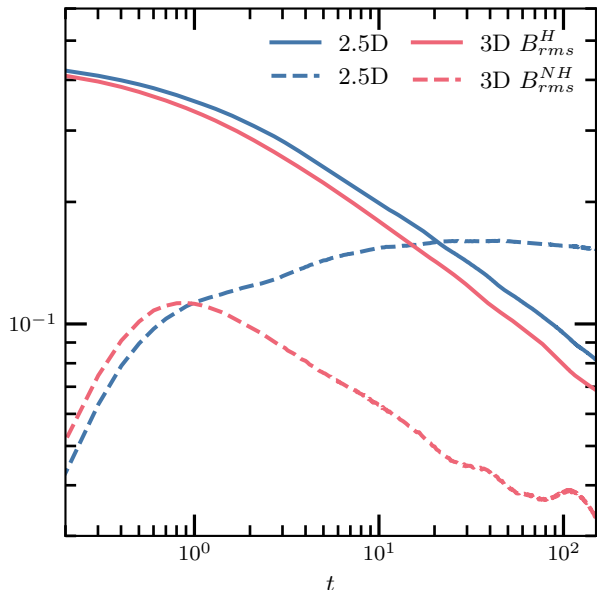


FIG. 3.— Comparison of evolution curves for B_{rms}^H from helical 2.5D and 3D runs at the same value of $S = 800$.

Thus, with Eqs. (9) and (10), we obtain $E_M \sim t^{-4/7}$ scaling. This scaling using τ_{rec} was recently also derived by Hosking & Schekochihin (2021). We find that this scaling bears out in both 2.5D and 3D simulations as is seen in Figs. 1 and 2. This further strengthens the idea that magnetic reconnection drives the decay and leads to the inverse transfer of energy in this system.

An important point deserving of attention is that the scaling of magnetic energy with time is the same in both 2.5D and 3D, a fact that has not been adequately acknowledged. This cannot be a coincidence, given that such a similarity was also found in the case of nonhelical decaying MHD turbulence in BZL21. In Fig. 3, we show the evolution curves from both 2.5D and 3D simulations together to clearly see that the slopes match. The underpinnings of this similarity between 2.5D and 3D will be discussed in detail in a later section 3.2.4.

The reason we explicitly calculated the helical part of the B_{rms} is that in the 2.5D case, the nonhelical part has a non-trivial evolution curve and thus total B_{rms} is not dominantly helical throughout the simulation. In Fig. 3, we show the evolution curves (dashed lines) for the nonhelical part of the field, $B_{rms}^{NH} = \sqrt{2E_M^{NH}}$ computed by subtracting out the helical part of the energy from the total, $E_M^{NH} = E_M - E_M^H$. It can be seen that, in the 3D case, after an initial rise around $t \sim 1$, B_{rms}^{NH} gradually decreases until the end of the simulation. In contrast, in the 2D case, B_{rms}^{NH} shows growth over time. This growth is because even though vector-potential squared, $\int \langle A_z^2 \rangle dV$ is a conserved quantity in 2D, since it is actually a 2.5D simulation (and not strictly 2D), the other two components of the vector potential corresponding to B_z are allowed to grow as is shown in Fig. 4. However, from anti-dynamo theorems, we expect this growth to cease and B_z should also decay ultimately (Shukurov & Subramanian 2021).

At this point, it is important to observe that if we were to write down the MHD equations separately for the component of the fields which are in-plane separately (i.e. fields that

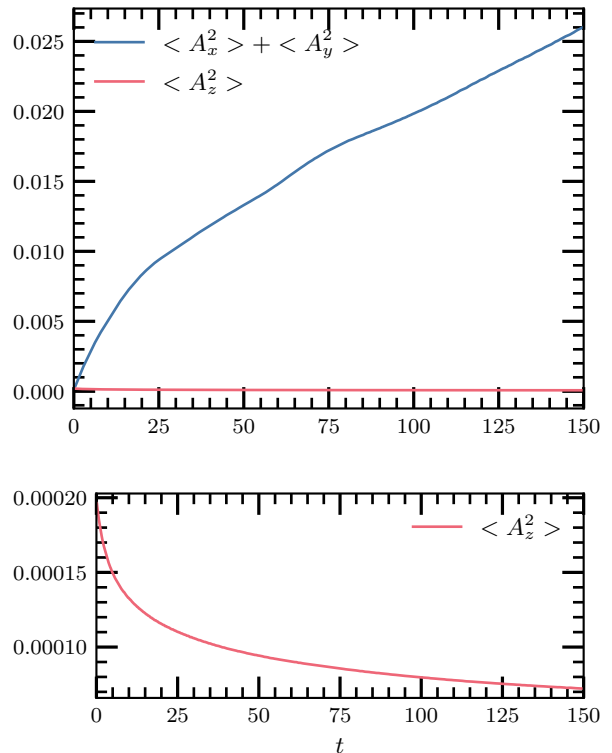


FIG. 4.— Evolution of $\langle A_x^2 + A_y^2 \rangle$ and $\langle A_z^2 \rangle$ from 2.5D helical run at 1024^2 resolution with $S = 800$.

are perpendicular to z and thus can be denoted as B_\perp), they exactly match with equations for a strictly 2D case and thus one expects from anastrophy conservation due to $\langle A_z^2 \rangle$ (also seen from Fig. 4), a scaling law,

$$B_\perp k_p^{-1} \sim const. \quad (11)$$

While this is true, only B_\perp component evolution is constrained by Eq. (11) and ultimately, it is the magnetic helicity which will constrain the evolution of B_z and B_\perp simultaneously and thus the primary scaling law is given by,

$$B_z B_\perp k_p^{-1} = B_{rms}^H k_p^{-1} \sim const. \quad (12)$$

The implications of the two Eqs. (11) and (12) are that $B_z \sim const.$ and $B_\perp \sim t^{-4/7}$. If, instead, one were to take Eq. (11) to be the primary scaling law, one would obtain $B_\perp \sim t^{-1/2}$. We confirm in Fig. 6, that simulation data verifies the decay exponents of $-4/7$ and $-2/7$ for B_\perp and B_{rms}^H respectively instead of $-1/2$ and $-1/4$.

Nonetheless, it is interesting that in the 2.5D case, nonhelical energy is produced in a system trying to achieve relaxation via reconnection. So, in fact, the total field decays at a much slower rate. In the 3D case, nonhelical energy is not produced as much. Thus, the decay of the total field reflects mainly the evolution of the helical component, which, as we have mentioned earlier, has the same scaling in time as seen in the 2.5D case.

In the 2.5D case, the contour plots of the vector potential A_z strung into a movie ⁴ show the merging of the magnetic

⁴ The link to 2.5D helical 4096² simulation movie: [A_z contour plots](#).

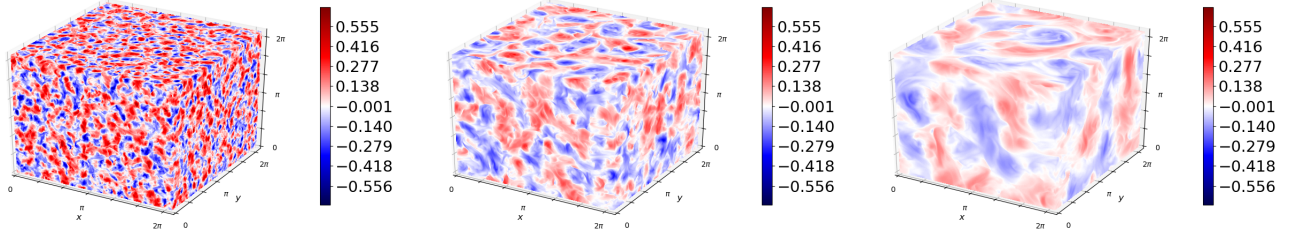


FIG. 5.—: Evolution of B_z on 3D domain from 3D helical (1024^3 , $S = 800$) run at times $t = 2, 12$ and 46 from left to right.

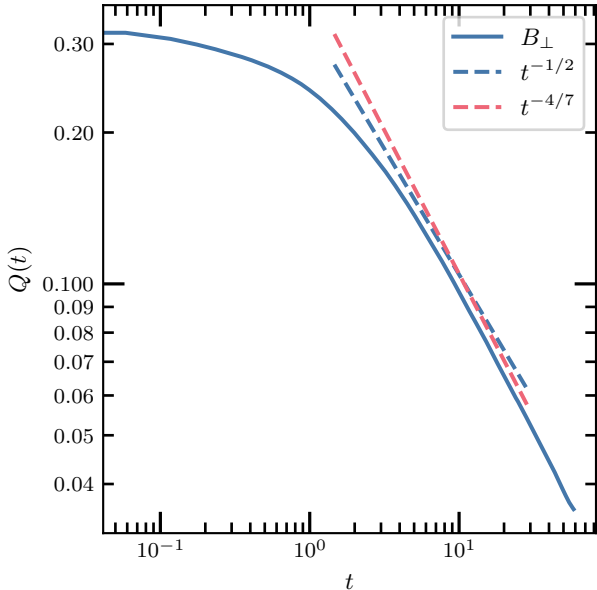
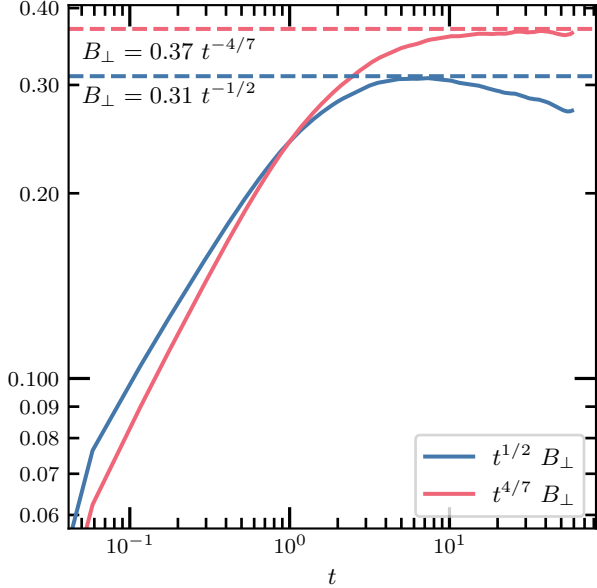


FIG. 6.—: Evolution curve for perpendicular component of \mathbf{B} for a 4096^2 helical run with $S = 800$, showing that B_\perp decays as $t^{-4/7}$.

islands with time. Localized current sheets form between two merging islands, leading to magnetic reconnection and, thus,

larger islands. Similarly, plots of magnetic structures on a 3D domain at a range of time instances for each magnetic field component [B_x, B_y, B_z] from helical 3D simulations are strung into a movie ⁵. This movie shows initial small-scale magnetic structures, moving with the turbulent flow merging with the localized neighbouring like-signed structures, thereby forming larger structures with the evolution of time as seen in Fig. 5. The structures merge likely via magnetic reconnection, leading to an inverse transfer of magnetic energy.

3.2. The case of nonhelical decaying turbulence

In BZL21, the study of 3D nonhelical decaying turbulence to investigate the possibility of magnetic reconnection driving the system was motivated by the similarity of the numerical result of $E_M \sim t^{-1}$ between 2D and 3D. In the 2D case, it is clear that the system is driven by reconnection. Additionally, vector-potential squared is not only ideally conserved but also better conserved than magnetic energy in the limit of large Lundquist numbers. One can do a similar calculation as we did in section 3.1 using Eq. (9) and the constraint obtained from the conservation of vector-potential squared or anastrophy,

$$E_M k_p^{-2} \sim \text{const.}, \quad (13)$$

to obtain the scaling law, $E_M \sim t^{-1}$.

In BZL21 it was claimed that conservation of anastrophy in Eq. (13), holds in 3D as well. To this end, BZL21 showed numerically that vector-potential squared is better conserved than magnetic energy in 3D. However, this result was overlooked in Hosking & Schekochihin (2021) with the claim, "this will be true for any decay satisfying $B^\alpha L \sim \text{const.}$ for any $\alpha > 0$ ", where L is a proxy for $1/k_p$ or L_{int} . We explicitly compare in a later subsection the rate of decay of various quantities and are able to make critical conclusions that go beyond the considerations specified above.

In Hosking & Schekochihin (2021), they instead introduced a new quantity, termed the Saffman helicity invariant,

$$I_H = \int \langle h(\mathbf{x})h(\mathbf{x} + \mathbf{r}) \rangle d\mathbf{r}, \quad (14)$$

where $\langle \rangle$ represents an ensemble average and claimed that this is the invariant which governs the scaling laws in the non-helical case. Their idea here is that a realistic system of MHD turbulence will contain helical fields of both polarities, resulting in zero net helicity. The integral I_H which measures the correlation in the magnetic helicity density, is expected to be ideally conserved and drive the nonhelical decaying system at large Lundquist numbers. Using this, they obtain the following power law, $E_M \sim t^{-1.18}$, which is actually quite different from t^{-1} measured in past numerical simulations (Zrake 2014;

⁵ The links to 3D helical 1024^3 sim movie: B_x, B_y, B_z .

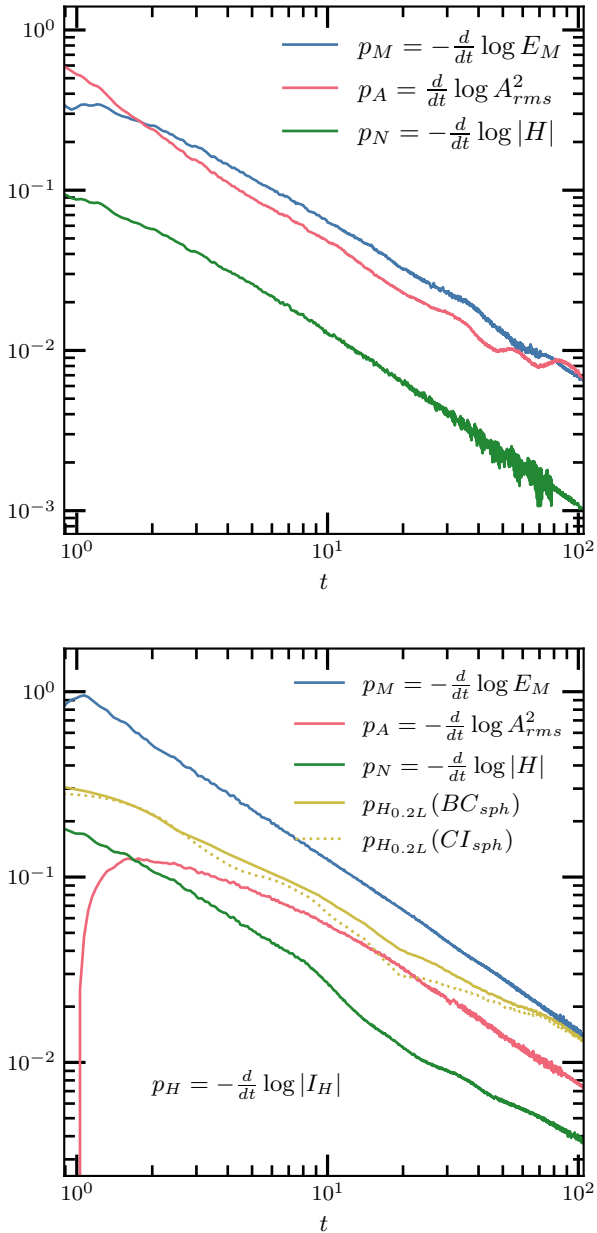


FIG. 7.—: Decay rates from 3D helical (upper panel) and nonhelical runs (lower panel). The integral I_H was evaluated using both methods of box-counting (BC) and correlation-integral (CI) evaluated in a spherical (sph) region with radius $R = 0.2L$. The decay rate of $\langle A^2 \rangle$ is lower than that of I_H in the nonhelical case, indicating that former is the better conserved quantity.

Berera & Linkmann 2014; Brandenburg et al. 2015; Reppin & Banerjee 2017; Bhat et al. 2021).

We have multiple reasons to conclude that I_H is not the underlying integral constraining nonhelical turbulence decay. We delineate these below.

3.2.1. Decay of the ideal invariants/conserved quantities

In the lower panel of Fig. 7, we show the rate of decay of magnetic energy, vector potential squared $\langle A^2 \rangle$, I_H and the total magnetic helicity, H_M . We find that while H_M is the

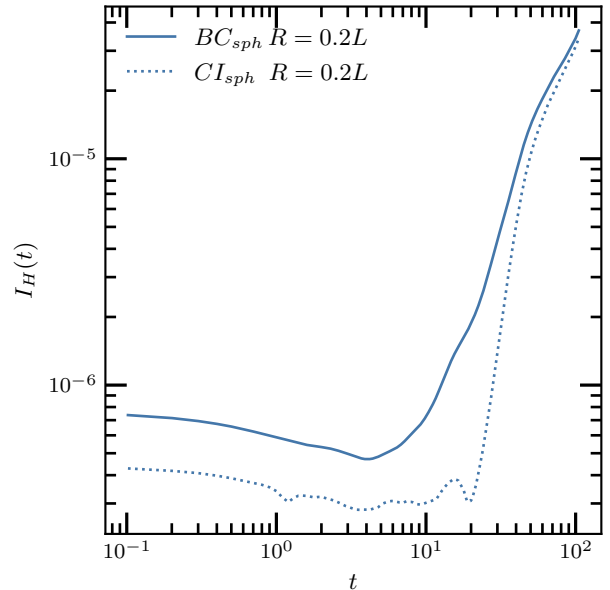


FIG. 8.—: Evolution of the integral I_H is evaluated by box-counting (BC) and correlation-integral (CI) methods in a spherical region with radius $R = 0.2L$ in the 3D helical run with 1024^3 resolution and $S = 800$.

slowest to change as expected, the next slowest is, in fact, $\langle A^2 \rangle$. Here, we have computed I_H using the same algorithms as provided in Zhou et al. (2022), available in PENCIL-CODE. In both methods of computing I_H at $R = 0.2L$, its rate of change is initially smaller than that of magnetic energy but larger compared to $\langle A^2 \rangle$. Eventually, the gap between the rate of change of I_H and that of the magnetic energy reduces, and this is likely because $k_p^{-1} \gtrsim R$. Thus, we find that I_H is not much slower than magnetic energy after around $t \sim 20$ and thus not as robustly conserved as $\langle A^2 \rangle$. We would like to further critically analyze the role of I_H in decaying MHD turbulence, which we do in the next subsection. As expected, in the upper panel of Fig. 7, H_M has the lowest decay rate. Notably, $\langle A^2 \rangle$ here actually grows instead of decaying (as we previously mentioned).

Another interesting thing to note is that in the helical case itself, I_H does not decay, but grows with time as can be seen in Fig. 8. This reveals that the integral I_H encodes the correlation scale of magnetic helicity. As the inverse transfer occurs, the integral scale shifts to larger values, indicating growth of helical structures to larger scales, which is also reflected in I_H .

3.2.2. Strength of helicity

The integral in Eq. (14) can be calculated in two different ways (Zhou et al. 2022). The one that is used in study of its invariance properties in Fig. 5 in Hosking & Schekochihin (2021) is to assume ensemble averages are equivalent to volume averages, where the averages are performed over volumes of size R ,

$$\begin{aligned}
 I_H(R) &= \frac{1}{V_R} \left(\int_{V_R} d^3r \int_{V_R} d^3x h(x)h(x+r) \right) \\
 &\equiv \frac{1}{VV_R} \int d^3x \left(\int_{V_R} d^3r h(x+r) \right)^2 \quad (15)
 \end{aligned}$$

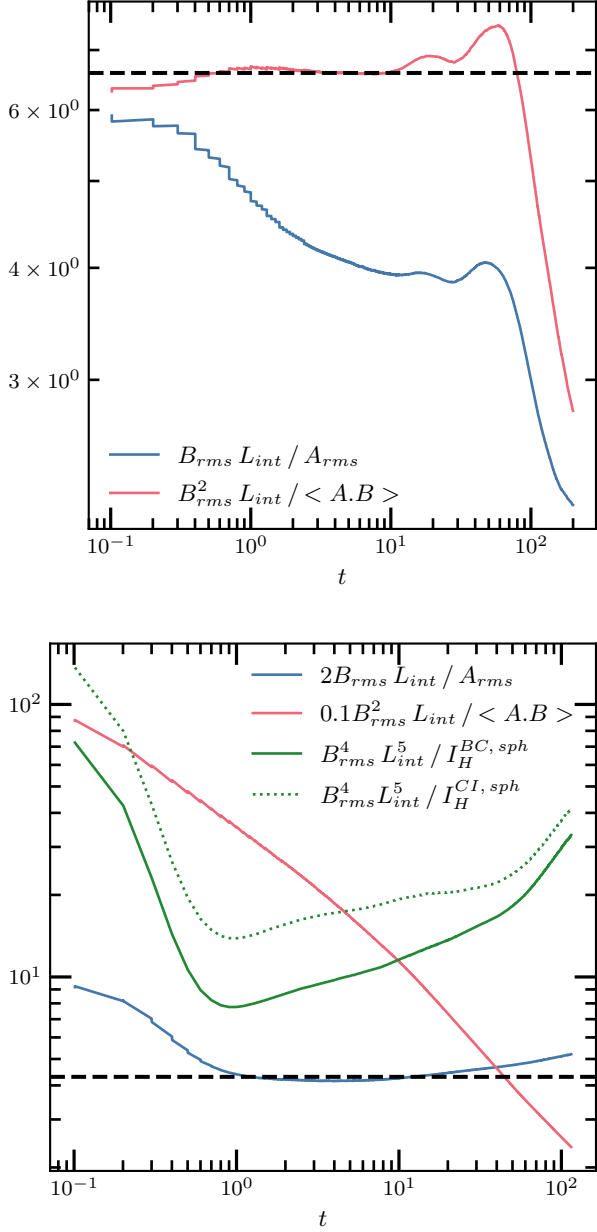


FIG. 9.—: Scalings from 3D (1024^3 , $S = 800$) runs. Upper panel: helical case, lower panel: nonhelical case. The ratio of $B_{rms}^4 L_{int}^5 / I_H$ (or equivalently, $E_M^2 k_p^{-5} / I_H$) $\gg 1$ indicating low strength in magnetic helicity in individual structures of opposite polarities.

The above is called the box counting method in Zhou et al. (2022). The second way to calculate the integral is to retain the inner correlation integral,

$$I_H(R) = \frac{1}{V} \left(\int d^3 r \int_{V_R} d^3 x h(x) h(x+r) \right). \quad (16)$$

The way $I_H(R, t)$ varies with R or t in these two ways of calculation is similar. This is because R is restricted to the range, $L_{int} \ll R \ll L$, where L is the system size.

An important difference between magnetic helicity or

vector-potential squared integrals and the I_H integral is that in the former case, the magnetic structures are assumed to be mostly limited to a narrow range in wavenumber $k \sim k_p$ (here $1/k_p \sim L_{int}$). Hence, the integral over the volume is superficial, and thus, the scaling does not include a L_{int}^3 factor. However, in the latter case, the integral over the volume is necessary to beget the scaling of $E_M^2 k_p^{-5} \sim const.$. This complicates the scaling relation as a simple dependence on a set of scales close to integral scale or the peak wavenumber k_p is not well justified.

However, our main criticism regarding the I_H integral is related to the strength of the helicity in the smaller structures. The strength of helicity is related to whether the given magnetic field structure is fully helical. The realizability condition requires, $k|H(k)|/2 \leq M(k)$. When $k|H(k)|/2 = M(k)$, the magnetic fields on that scale or wavenumber are fully helical. In helical decaying MHD turbulence, the reason we can apply the constraint in Eq. (10) is because the fields in the system are fully helical to begin with, which is the case in all the helical simulations in our paper as well as the previous ones. In fact, during the early part of the evolution, the fields remain fully helical, as we have seen already in Fig. 3, which shows that even though the nonhelical part grows, it is smaller compared to B_{rms}^H by more than an order of magnitude. However, the gap between the two curves keeps decreasing monotonically.

Thus, in the fully helical case, we can indeed assume $\langle A \cdot B \rangle \sim E_M L_{int} \sim const.$ is a good constraint. Similarly, in the nonhelical case, $I_H \sim E_M^2 L_{int}^5 \sim const.$ could be considered to robustly constrain the system evolution only if the individual magnetic structures of opposite polarities are fully helical. Our simulations show in the lower panel of Fig. 9 that indeed the strength of helicity is expectedly small in nonhelical turbulence and thus $E_M^2 k_p^{-5} / I_H \gg 1$ (or $B_{rms}^4 L_{int}^5 / I_H \gg 1$). This ratio (here I_H is measured at $R = 0.2L$) remains larger than an order of magnitude (if we consider the dashed curve) compared to a factor of ~ 2 in the case of the ratio $B_{rms} L_{int} / A_{rms}$. In the helical run as shown in the upper panel of Fig. 9, the ratio $B_{rms}^2 L_{int} / H_M \sim 2\pi$ (due to the factor in L_{int}), remains quite flat indicating the validity of usage of H_M to constrain the system. Note that the curves corresponding to the ratios of $B_{rms}^2 L_{int} / H_M$ (in upper panel) and $B_{rms} L_{int} / A_{rms}$ (lower panel) have initial amplitude around 6 due to the 2π factor in L_{int} . In the case of $B_{rms}^4 L_{int}^5 / I_H$, the volume cancels out and only $(2\pi)^2$ remains (due to squaring of helicity), which should have led to an initial amplitude of 40 if the structures were fully helical, but we get 100 instead (as opposed to no such extra factors in the case of anastrophy here or magnetic helicity in the fully helical case). In fact the ratio involving magnetic helicity, $B_{rms}^2 L_{int} / H_M$, is as large as ~ 1000 initially given that the system is nonhelical.

In Fig. 9, both curves corresponding to I_H and anastrophy dip initially in the transient phase. While the latter dips to a factor of 2 and remains flat from around $t = 1$ to $t = 40$, the former touches a value of 10 at $t = 1$ and then increases again. Thus, we find that $B_{rms}^4 L_{int}^5$ is not robustly represented by I_H due to the lack of strength in helicity.

Our argument gains additional support from Fig. 10. Here we present histograms of the cosine angle between the vector potential and the magnetic field, offering insights into their alignment. For fully helical fields, we obtain $\cos \theta = 1$ and for fully nonhelical fields, $\cos \theta = 0$. In the helical case of decaying MHD turbulence, as shown in the upper panel of

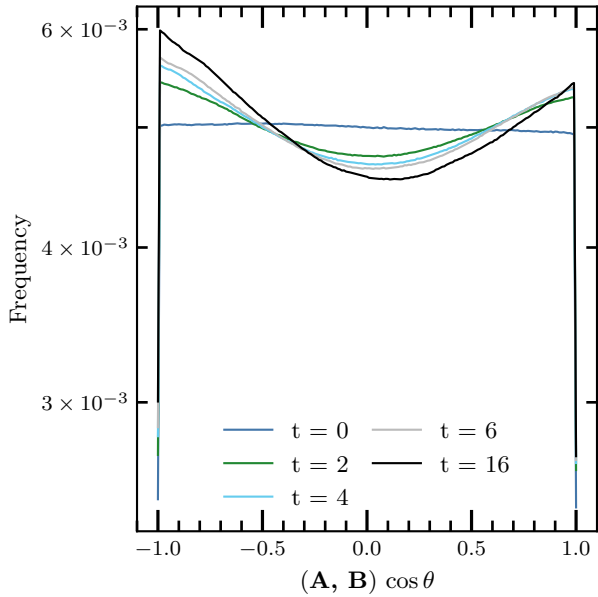
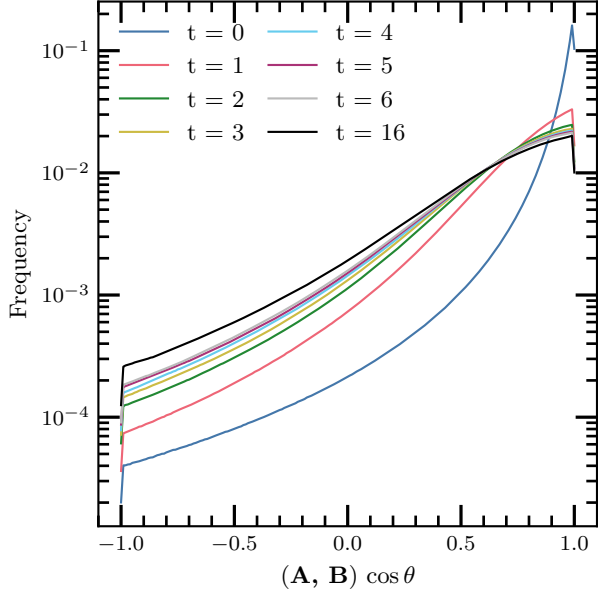


FIG. 10.—: Histograms of the cosine angle between the vector potential and the magnetic field from 3D (1024^3 , $S = 800$) runs. Upper panel: is the helical case showing a peak at +1 with frequency of ~ 0.1 and a sharp drop from there indicating that most of domain has fully helical fields (at all times). Lower panel: is the nonhelical case which is flat at $t = 0$. Peaks at values of ± 1 show up subsequently but with an incremental factor of only 1.18 indicating most of the domain is still largely nonhelical.

Fig. 10, the magnetic fields are initialized to be random and fully helical. As expected, nearly 90% of the total grid points (or counts) fall within the bins of $\cos \theta \in [0.8, 1]$, and a steep drop from the peak is observed. Consequently, the portion of the domain containing nonhelical fields is minimal, and this trend persists as the system evolves.

On the other hand, the lower panel in Fig. 10 shows the

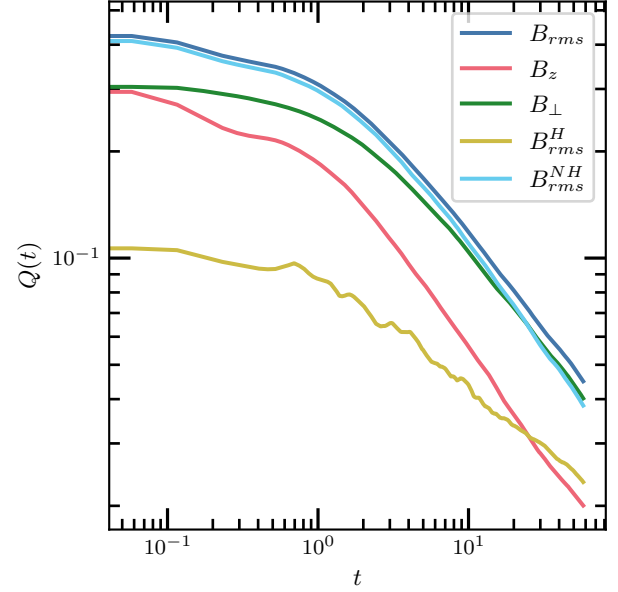


FIG. 11.—: Evolution of the components of \mathbf{B} for the nonhelical 2.5D case.

histogram for the nonhelical case. In this case, the field is initially random but with no helicity. Hence, the $t = 0$ curve is flat. According to the theory put forward by Hosking & Schekochihin (2021), the fully nonhelical fields should relax on a fast time scale, leaving the system with only helical fields. This decay should have manifested with peaks at both $\cos \theta = 1$ and $\cos \theta = -1$ and a sharp drop. However, we find that there is a development of such peaks on a long time scale (compared to the Alfvén scale), and this growth in amplitude is only a factor of about 1.18, which is insignificant. The growth of such a peak mainly happens because it is easier for diffusion to kill fields which are less helical. Even at $t = 16$, the percentage of points which lie within the set $\cos \theta \in [-1, -0.8] \cup [0.8, 1]$ is only about 25%. Additionally, we have checked that if we were to condition the histogram by the magnitude of the field i.e., we consider only those gridpoints where the field exceeds a threshold, say, fB_{rms} , where $f \geq 1$, the peaks are larger by only an incremental factor of about ~ 2 or so. Thus, we show that in the nonhelical system, the strength of helicity is low. Therefore, a helicity-based integral such as I_H likely cannot constrain the evolution of the system.

Another crucial point to underscore is that even though magnetic helicity H_M is well-conserved in also the nonhelical case (as evident in the lower panel of Fig. 7), we cannot use it to constrain the evolution of nonhelical system because the strength of helicity is insignificant. In a similar vein, I_H may function as a well-conserved quantity (with a slightly lower decay rate compared to magnetic energy) (Zhou et al. 2022), but its effectiveness in constraining the evolution of a nonhelical system remains questionable.

3.2.3. Strictly 2D case of nonhelical decay

The third reason for concluding that I_H is not important in decaying turbulence is related to the observation that, in both 2.5D and 3D, the helical and nonhelical cases show the same, decay in time, power laws. In the helical case, it is obviously the magnetic helicity conservation which plays the critical role in constraining the system's evolution in both

2.5D and 3D. Similarly, in the nonhelical case, we expect the same conserved quantity (thus leading to the same results) to constrain evolution in both 2.5D as well as 3D. A further interesting observation is that, in the nonhelical case, the same decay power law of $E_M \sim t^{-1}$ holds in the strictly 2D case as well ($B_z = A_x = A_y = 0$ throughout the simulation). In the 2D case (as opposed to 2.5D), magnetic helicity is not well-defined. Thus, any integral based on magnetic helicity is ruled out, including the Saffman helicity integral, I_H . Evolution plots from strictly 2D simulations with $E_M \sim t^{-1}$ were already seen in Fig. 1 of BZL21. There, we also confirmed that the strictly 2D simulations were similar to 2D simulations using the reduced-MHD model in Zhou et al. (2019). Thus, only vector-potential squared can explain the decay power law in the 2D case. And its influence extends to the 3D case as well, similar to magnetic helicity in the helical case.

A further piece of evidence in favor of vector-potential squared $\langle A^2 \rangle$ is seen in Fig. 11. Here, we show different components of the magnetic field in a 2.5D nonhelical decaying turbulence system. We find that the system relaxes such that B_z decays on a faster time-scale, making the in-plane component the dominant one. Such a behaviour could manifest also in 3D locally around sites of reconnection (where most of the action takes place). Thus, we find it is not only $\langle A_{2D}^2 \rangle$ (see SM of Brandenburg et al. (2015)) but even $\langle A^2 \rangle$ which is conserved.

3.2.4. Local anisotropy

The question, then, is why there is a match between 2D (or 2.5D) and 3D results. Such a question was already posed in BZL21. The 2D-3D match has turned out to be more general, extending to the helical case as well. We continue to think that a quasi-two-dimensionalization is involved, in the sense that the individual magnetic reconnection events seem to manifest in a 2D fashion within the 3D domain. In the reconnection literature, a quasi-two-dimensionalization manifests typically in the presence of a guide field, i.e. the reconnection rates are similar between a 2D case and a 3D case with a guide field. We resort to the well-known idea that local mean fields in the system can provide a local guide field for small-scale fields leading to local anisotropy (Cho & Vishniac 2000). We study such possibilities using Minkowski functionals in the next section.

4. QUANTIFYING MAGNETIC FIELD ANISOTROPY USING MINKOWSKI FUNCTIONALS

Minkowski functionals (MFs) are tools which can be used to find the morphology of structures in a scalar field. It can help identify whether the isosurfaces in a given dataset are planar or filamentary, etc. The system of interest in this paper is magnetically dominated decaying MHD turbulence, which does not contain a guide field. Thus, it is not obvious if there can be anisotropy in the system, at least locally. But from our analysis in previous sections, we have provided ample evidence which suggests the possibility of quasi-two-dimensionalization of the 3D system at the relevant scales where magnetic reconnections occur. This likely includes the integral length scale (or the scales corresponding to the peak wavenumber k_p) and the smaller scales. Since we posit that reconnection in the 3D system manifests in a 2D fashion, from the previous literature, we gather that the reconnecting structures need to be influenced by a local guide field or mean field. Depending

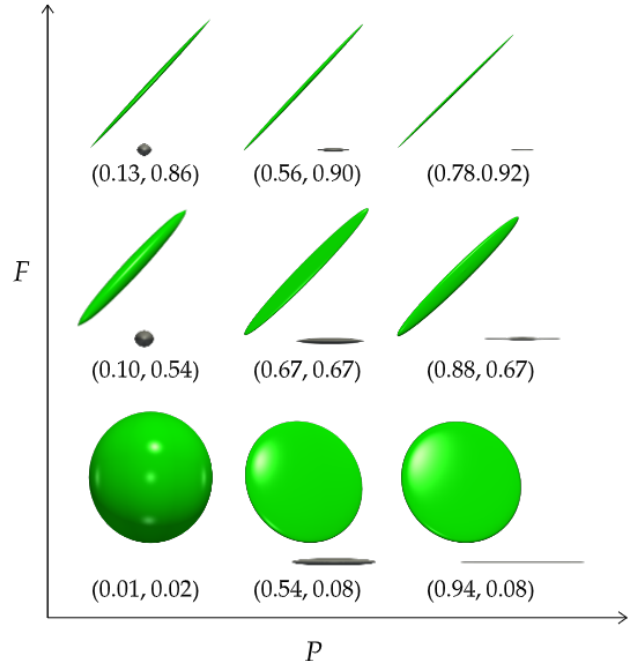


FIG. 12.— Known as the Blaschke diagram, we show the morphology of different spheroids as values of P and F varies along the abscissa and the ordinate respectively.

on the physics and the presence of local guide/mean fields, the magnetic structures can be rendered anisotropic in their morphology. We would like to use Minkowski functionals to detect and measure this anisotropy.

We can test for quasi-two-dimensionalization by quantifying the spatial correlation of magnetic fields near reconnection sites in the computational domain. In such a quasi-2D scenario, the magnetic fields are expected to be correlated preferentially along one direction over the other two. That is, the fields should be anisotropic locally around the reconnection sites.

We first identify reconnection sites and then detect the magnetic fields around these sites. The necessary condition for reconnection to occur is the presence of high current density (see Priest (2016) for sufficient conditions). Around a given high current density site, we analyze the correlation of magnetic fields by assessing the morphology of isonorm surfaces of $|\mathbf{B}|$. The information regarding the shape of the isonorm surfaces is extracted using Minkowski Functionals (MFs). Mecke et al. (1994) first introduced MFs in cosmology, and these were later employed by many others for morphological feature extraction (Refer to Sheth et al. (2003) for a complete review of MFs). The execution of Minkowski functionals we employ is in Python from Sheth et al. (2003), who use the shape finders introduced by Sahni et al. (1998). The four Minkowski functionals are defined as,

$$\begin{aligned} V_0 &= \iiint dV & V_1 &= \frac{1}{6} \iint dS \\ V_2 &= \frac{1}{6\pi} \iint (\kappa_1 + \kappa_2) dS & V_3 &= \frac{1}{4\pi} \iint \kappa_1 \kappa_2 dS \end{aligned} \quad (17)$$

where κ_1 and κ_2 are the two principal curvatures. The volume and surface integrals, respectively, in the equations above, are specified over closed isosurfaces for a given field. We can

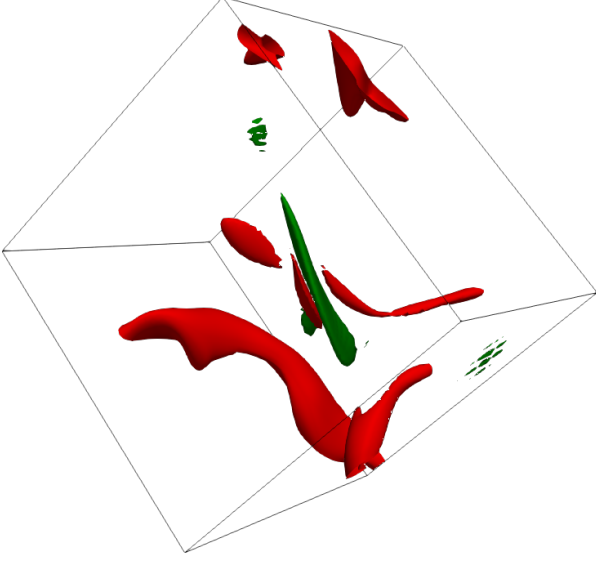


FIG. 13.— Zoomed in version of isosurfaces of the current density $|\mathbf{J}|$ and the magnetic field $|\mathbf{B}|$ are shown in green and red respectively from the nonhelical run of 1024^3 with $S = 800$. The domain size shown here is 72^3 .

extract three length scales from V_0, V_1, V_2 and V_3 . The typical thickness, width, and length derived from (17) are,

$$T = \frac{V_0}{2V_1}, \quad W = \frac{2V_1}{\pi V_2}, \quad L = \frac{3V_2}{4V_3}. \quad (18)$$

These three length scales are ordered such that $l_1 = \max(T, W, L)$, $l_2 = \text{mid}(T, W, L)$, $l_3 = \min(T, W, L)$. Next, we can obtain planarity and filamentarity for a given isosurface structure as follows,

$$P = \frac{l_2 - l_3}{l_2 + l_3}, \quad F = \frac{l_1 - l_2}{l_1 + l_2}. \quad (19)$$

To both validate our implementation of the MFs and provide an understanding of the morphology of structures in a phase space governed by P and F , we show the Blaschke diagram in Fig. 12. Here, the abscissa varies over planarity P , and the ordinate varies over filamentarity F . It is clear from Eq. (19) that the range of P and F is $[0, 1]$, where zero means no planarity or no filamentarity. In Fig. 12, we show how the shapes change depending on the values of (P, F) . We have a sphere in the lower left corner of the plot that changes to a plate as P increases (with F constant) in the lower row but changes to a rugby ball-like shape as F increases (with P constant) in the left column.

Further, we have also performed the MF analysis separately for fully developed hydrodynamic turbulence and confirmed the expected results. This can be found in appendix E.

Since magnetic reconnection occurs near points where there is a significant value of current density, we implement an algorithm to obtain isolated clusters of points with the current density value $|\mathbf{J}|$ exceeding a threshold of $0.7|\mathbf{J}|_{\max}$. In each such cluster, we designate the point with the highest value as the representative point. We designate the current density isosurface with isovalue of $0.5|\mathbf{J}|_{\max, \text{cluster}}$ as our fiducial current sheet for that cluster.

Next, we would like to obtain a set of magnetic field iso-

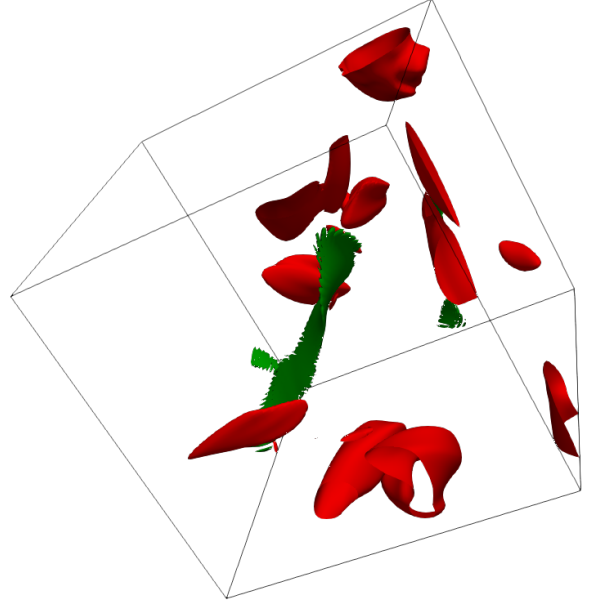


FIG. 14.— Zoomed in version of isosurfaces of the current density $|\mathbf{J}|$ and the magnetic field $|\mathbf{B}|$ are shown in green and red, respectively, from the fully helical run of 1024^3 with $S = 800$. The domain size shown here is 116^3 .

surfaces close to this current sheet. So, we employ a range of isovalues to do this. To determine this range of isovalues, consider the following scheme. Around a *current sheet* (in an isolated cluster), $|\mathbf{B}|$ is calculated along rays emanating from the representative point. Once we obtain the $|\mathbf{B}|$ profile around the representative point, we find the maximum and minimum value of $|\mathbf{B}|$ nearest to the point. Then we use these extrema values to determine a range of isovalues of $|\mathbf{B}|$ given by,

$$|\mathbf{B}|_{\max} - \frac{i}{5} \times \left(\frac{|\mathbf{B}|_{\max} - |\mathbf{B}|_{\min}}{4} \right) \quad \forall i \in 1, 2, 3, 4, 5. \quad (20)$$

Thereafter, Minkowski functionals for $|\mathbf{J}|$ and $|\mathbf{B}|$ surfaces are calculated, and their evolution with time is reported. The details of algorithm for MFs implementation and the scheme we described briefly for obtaining isosurfaces is available in Appendix B and C.

4.1. Results for Minkowski functionals

For an illustration, we show in Figs. 13 and 14 the isosurfaces of an isolated current density structure corresponding to a possible reconnection site and also isosurfaces of the magnetic fields nearby that are potentially participating in the reconnection. We calculate the MFs for such structures of current density and the magnetic field throughout the domain of the 1024^3 runs of $S = 800$ in both helical and nonhelical cases. We extract the quantities l_1, l_2, l_3 and the corresponding P and F values. Below, we study their distributions (histograms) and evolution in time.

4.1.1. Nonhelical case

In Fig. 15, we show the histograms of the measured planarity P and filamentarity F at a given time, $t = 5$ from the 1024^3 run of $S = 800$. In these charts, NVC (no-volume-cutoff) denotes the histogram for the complete set of structures. The darker

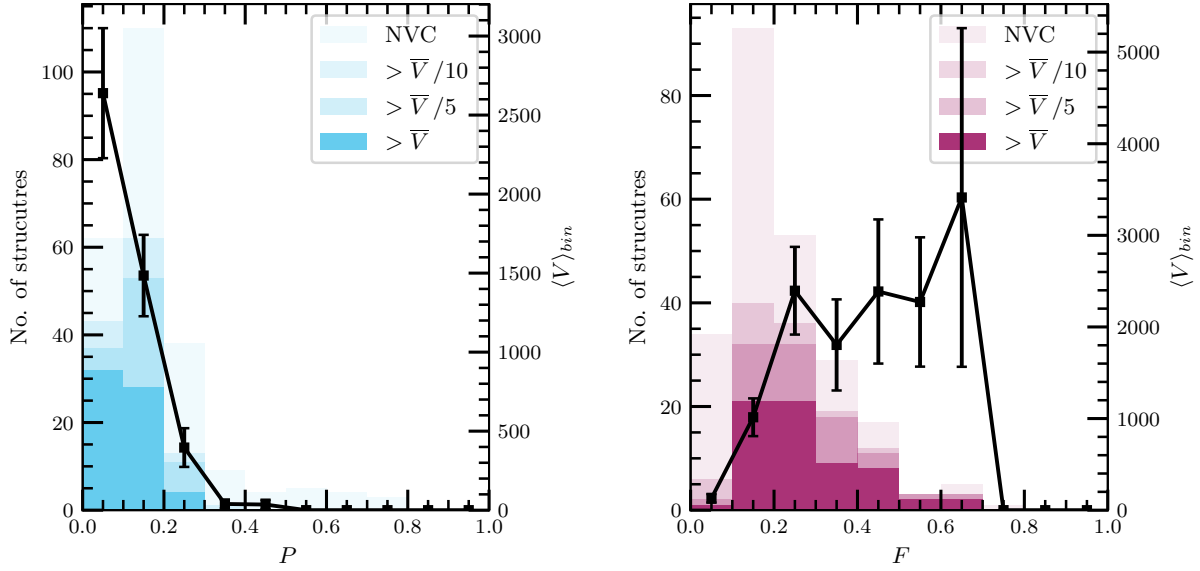


FIG. 15.— **Nonhelical:** Histogram for planarity (left panel) and filamentarity (right panel) of all the *reconnecting magnetic field structures* in the nonhelical 1024^3 simulation with $S = 800$, at $t = 5$. Also shown in the black squares is the average volume in each bin. NVC stands for no-volume-cutoff. The darker shades represent statistics for structures considered above a certain volume threshold denoted by \bar{V}/n and $n = 1, 5$ or 10 . The tendency of large structures to have smaller planarity and larger filamentarity is clear from the graph. The same conclusion can also be reached by progressively considering structures with larger and larger volumes, as we have shown in this plot.

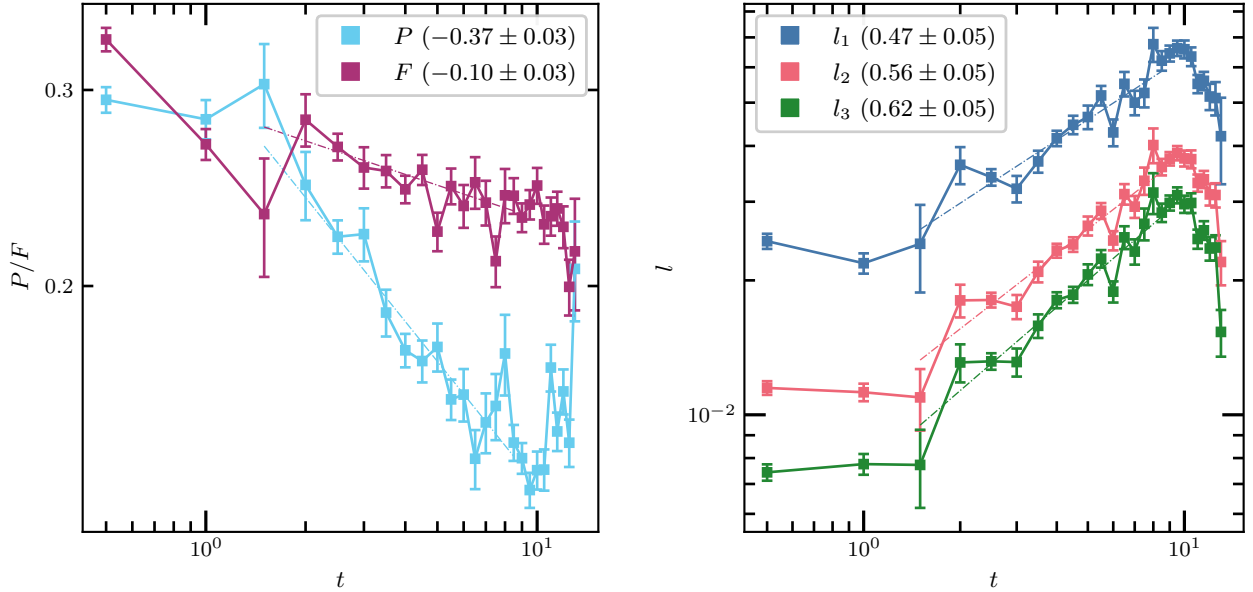


FIG. 16.— **Nonhelical:** Time evolution of P and F in the early stages of the decay (when the B_{rms} curve behaviour is close to the theoretical prediction of $t^{-0.5}$), is shown in the left panel. The time evolution of length scales of *reconnecting magnetic field* isosurfaces is shown in the right panel. The different dashed curves are the least square fit, and they indicate a scaling close to the expected $l \sim t^{1/2}$.

shades correspond to histograms derived from a subset where only structures with a volume surpassing a specific threshold are considered. The darkest shade represents the subset where only structures with a volume exceeding the average value \bar{V} are considered. The planarity histogram (left panel of Fig. 15) peaks within the bin of 0.1–0.2. With subsets of larger volume structures, the histograms progressively shrink towards lower values of P . This indicates the tendency of more voluminous structures to have smaller planarity. In the case of filamentarity histogram (right panel of Fig. 15), the peak is within the bin of 0.2–0.3. Here, as we limit the set to having more voluminous structures, the average value of F shifts to the higher side. On the whole, the structures are more filamentary than planar. These values indicate that the structures feature between the sphere and the middle ellipsoid in the first column of the Blaschke diagram in Fig. 12. Thus, their geometry is akin to prolate spheroids, which are more filamentary than they are planar (unlike the oblate spheroid). This kind of anisotropy inherent in the magnetic structure is likely reflective of the local anisotropy within the system.

Next, we study the evolution of the morphology of the structures. In the left panel of Fig. 16, we show the evolution of the average value of P and F calculated for the magnetic fields. Firstly, both P and F tend to decrease. This can be understood as the increasing effect of diffusion, which tends to even out the structures. While the decrease in F is very small ($\sim t^{-0.1}$ given by a straight line fit as mentioned in the legend), the decrease in P is larger. Here, the P and F values were calculated by taking the average of the values obtained from all the individual isosurfaces (detailed steps are in Appendix C). These average P and F values do not have to necessarily match with that resulting from the average values of l_1 , l_2 and l_3 (let us call them P^* and F^*), and indeed they don't. However, the trends match, though the indices of power law decay are different, i.e. $P^* \sim t^{-0.25 \pm 0.03}$ and $F^* \sim t^{-0.2 \pm 0.04}$.

The behaviour of P^*/P and F^*/F is roughly consistent with the power law growth of l_1 , l_2 and l_3 as shown in the right panel of Fig. 16. The thin dashed lines indicate a straight line fit to the evolution curves, and we infer the respective power-law indices. It can be seen that indeed l_2 and l_3 increase faster than l_1 . This can be understood as the effect of diffusion, which acts more efficiently on smaller scales. Thus, the indices increase progressively as we go from l_1 to l_3 . Otherwise, the values of the power law indices (within the error bars) are close to the theoretically expected value of 0.5 (more so for l_1 and l_2 than l_3 , which is most affected by diffusion). It's important to note that the accuracy of the straight line fit is influenced by the chosen time range. Nevertheless, we demonstrate that a fit closely aligning with the theoretical expectation is not unreasonable, considering the estimated error bars.

4.1.2. Helical case

Next, we consider the iso-surfaces in the decaying helical MHD turbulence. In Fig. 17, we once again show the histograms of the measured planarity P and filamentarity F at a given time, $t = 5$ from the helical 1024^3 run of $S = 800$. The peak of the planarity histogram, similar to that of the non-helical case, peaks within the bin of 0.1 – 0.2. However, the filamentarity histogram peaks at a larger value within the bin of 0.3 – 0.4 for more voluminous structures. Here again, as we restrict to a subset of structures with larger volumes, the averages shift to lower values for P and higher values for F . As in the nonhelical case, the structures are more filamentary

(even more so) than planar.

In the left panel of Fig. 18, we show the evolution of the average value of P and F to assess how the morphology of the structures changes. Here, F is nearly constant as time evolves, whereas the value of P shows a decrease (similar to the nonhelical case) with time. In the right panel of Fig. 18, we show the evolution of l_1 , l_2 and l_3 and we find here the decay of l_2 and l_3 are not all that much faster than l_1 (unlike the nonhelical case). We can chalk up this behaviour and constancy of F to the fact that helical structures tend to be more resilient to diffusion (Bhat et al. 2014). Here again, we find that the power law indices from the straight line fit, as shown are close to the theoretically expected value of ~ 0.57 .

MF analysis was also performed for the current density structures. In Fig. 19, we show the phase space Blaschke plot for P and F values from all the different cases of helical MHD, nonhelical MHD and hydrodynamics (no magnetic fields). Here, the values of (P, F) for the current density structures (shown in a diamond shape) are around $\sim (0.53, 0.5)$ in the helical case and $\sim (0.45, 0.37)$ in the nonhelical case. Thus, unlike the case of magnetic field isosurfaces, the current density structures appear between the bottom two structures in the middle column of the Blaschke diagram in Fig. 12. Thus, they are largely sheet-like, reaffirming the understanding of this system as a quasi-2D system with 2D-like reconnections.

5. A QUASI-2D HIERARCHICAL MERGER MODEL

A hierarchical merger model was first proposed in Zhou et al. (2019) to understand a 2D system is driven by island mergers due to coalescence instability. It was useful to derive scaling laws associated with the decay of magnetic energy and resulting inverse transfer. While BZL21 suggested that the 3D decaying MHD turbulence is akin to the 2D system (also with similar scaling laws), but they didn't provide a 3D model to describe the system. A 3D model was proposed in Zhou et al. (2020), but it was for a system with a uniform mean field or guide field. We find that their hierarchical model is incompatible with what we propose below.

In our quasi-2D hierarchical merger model (Q2DHM model), interactions between magnetic structures happen pairwise. An interaction consists of magnetic reconnection at the interface, leading to a merger. Such a merger, then, conserves mass and magnetic flux or magnetic helicity (depending on the system). The resulting structures are then a size larger but with a lower strength of magnetic field. Thus, the two ingredients which were required to solve the Kolmogorov-type calculation using decay equation in Eq. (9) is available in the Q2DHM model as well : (i) the reconnection timescale being the driving timescale for the system, (ii) a conserved quantity to constrain the relationship with the magnetic field and the integral scale in the problem. However, the advantage of the Q2DHM model over the decay equation in Eq. (9) is that it allows us to make the distinction between a 2D and a 3D system and explicitly see the manifestation of quasi-two-dimensionality.

In the model, the mergers happen in discrete stages (given by n). A key assumption is that at any given stage, there is uniformity in magnetic field structures, i.e. all of them have the same dimensions of l_{1n} , l_{2n} and l_{3n} . The magnetic field in a structure is given by B_n .

First, the merger of two structures conserves mass. Assum-

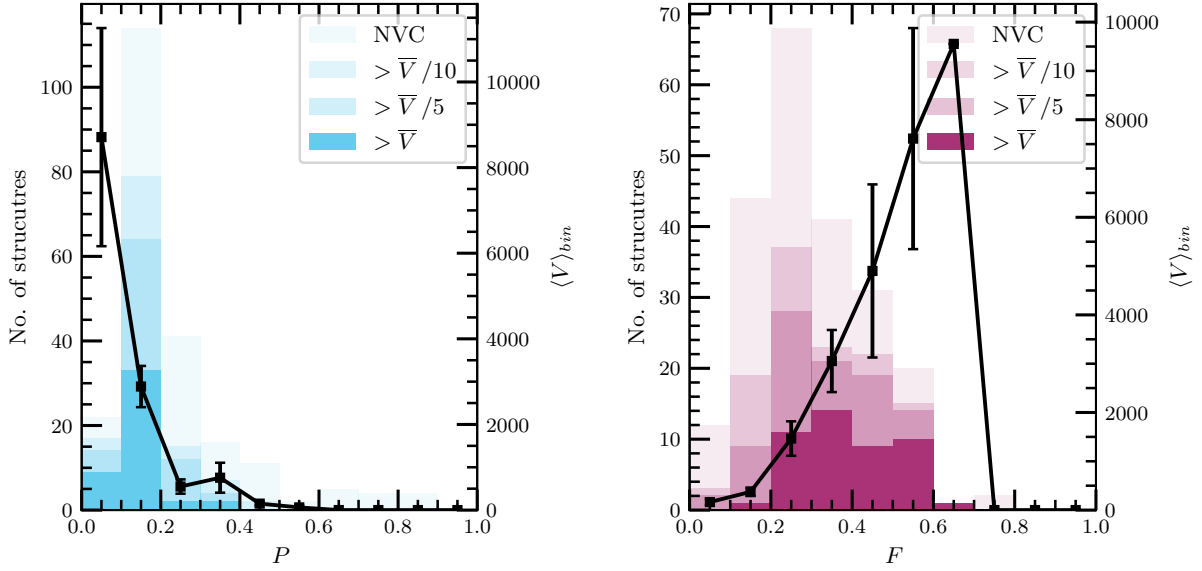


FIG. 17.— **Helical:** Histogram for planarity (left panel) and filamentarity (right panel) of all the *reconnecting magnetic field structures* in the helical 1024^3 simulation with $S = 800$, at $t = 5$. Also shown in the black squares is the average volume in each bin. NVC stands for no-volume-cutoff. The darker shades represent statistics for structures considered above a certain volume threshold denoted by \bar{V}/n and $n = 1, 5$ or 10 . The tendency of large structures to have smaller planarity and larger filamentarity is clear from the graph. The same conclusion can also be reached by progressively considering structures with larger and larger volumes, as we have shown in this plot.

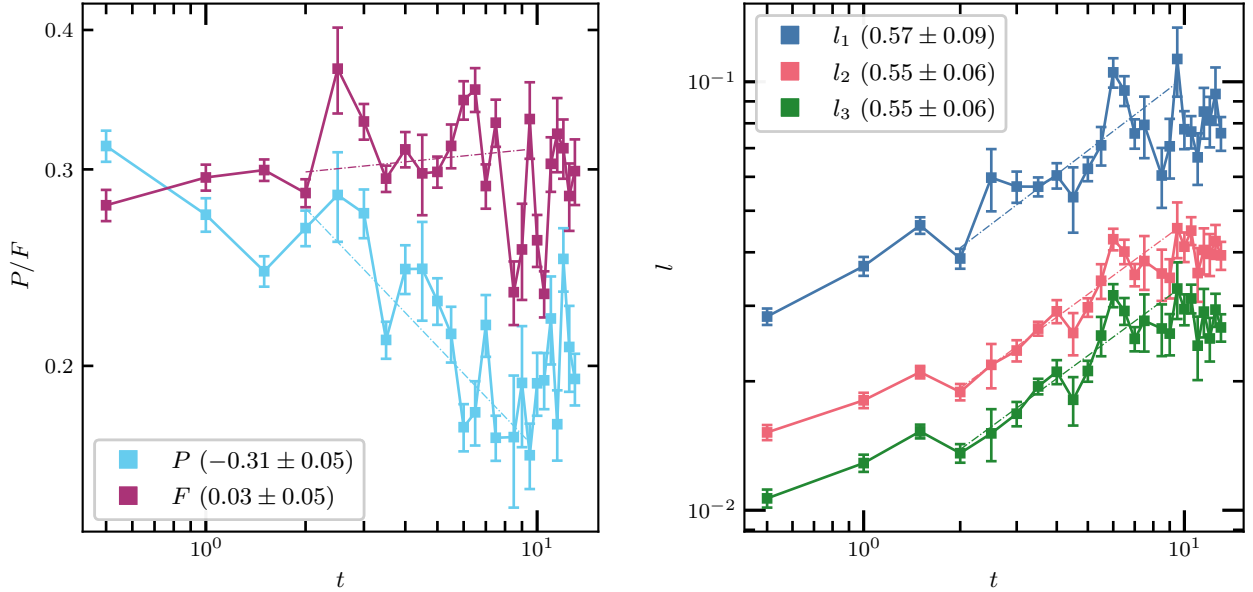


FIG. 18.— **Helical:** Time evolution of P and F in the early stages of the decay (when the B_{rms} curve behaviour is close to the theoretical prediction of $t^{-2/7}$), is shown in the left panel. The time evolution of length scales of *reconnecting magnetic field* isosurfaces is shown in the right panel. The different dashed curves are the least square fit, and they indicate a scaling close to the expected $l \sim t^{4/7}$.

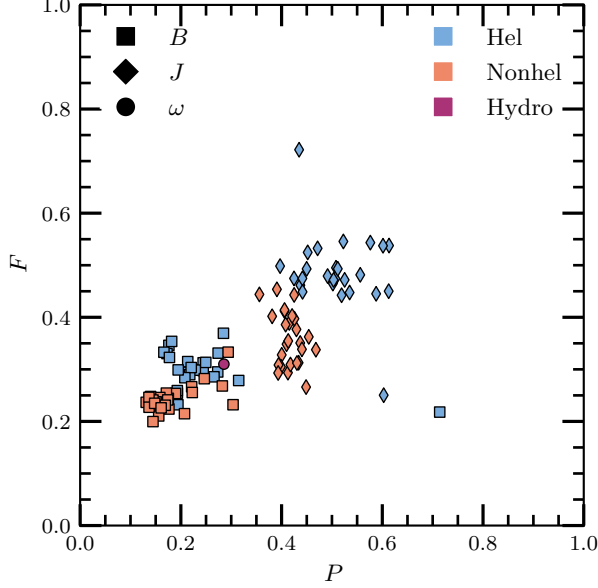


FIG. 19.— Blaschke plot of the combined helical, nonhelical, and hydrodynamic simulations. The (P, F) of the vorticity of the forced hydrodynamic simulation has been given as a reference point against which the (P, F) of the MHD simulations could be compared. Note that there is an outlier in the (P, F) of the magnetic field in the helical simulation at $(0.71, 0.22)$ which occurs at $t = 8$. This is because there was only one current sheet above the threshold, so we could not obtain enough statistics. We ignore this data point in the evolution plots.

ing the condition of incompressibility, we can write,

$$2l_{1n}l_{2n}l_{3n} = l_{1n+1}l_{2n+1}l_{3n+1} \quad (21)$$

where $n + 1$ denotes the next stage (or the next generation). Thus, we have $l_{1n+1} = 2^{1/3}l_{1n}$, $l_{2n+1} = 2^{1/3}l_{2n}$ and $l_{3n+1} = 2^{1/3}l_{3n}$.

Second, we demand flux conservation. However, for a system with quasi-two-dimensionality, the structures reconnect on a plane guided by a local mean field, then the conservation of flux can be given by,

$$B_n l_{in} \sim \text{const.} \quad (22)$$

where the i subscript can assume 1, 2 or 3 depending on the plane of reconnection. Thus, we have $B_{n+1} = 2^{-1/3}B_n = 2^{-n/3}B_0$, where B_0 is the initial field. We can now calculate the Lundquist number at the $n + 1$ stage,

$$S_{n+1} = \frac{B_{n+1}l_{in+1}}{\eta} = \frac{2^{-1/3}B_n 2^{1/3}l_{in}}{\eta} = S_n \quad (23)$$

Since each merger is driven by reconnection, the corresponding timescale is given by the inverse of the reconnection rate. Since we assume the 2D steady-state model of Sweet-Parker for reconnection, we obtain,

$$\tau_{recn+1} = S_{n+1}^{1/2} \tau_{A_{n+1}} = 2^{2/3} \tau_{A_n} = 2^{2n/3} \tau_0 \quad (24)$$

The time taken to reach the n th generation can be approximated to be $t_n \approx 2^{(2/3)n} \tau_0$, for large n . Thus we have time $\tilde{t} = t_n / \tau_0 = 2^{(2/3)n}$. Now, we can eliminate n to obtain time dependence

of various quantities,

$$\begin{aligned} B &= B_0 \tilde{t}^{-1/2}, & l_1 &= l_{10} \tilde{t}^{1/2} \\ l_2 &= l_{20} \tilde{t}^{1/2}, & l_3 &= l_{30} \tilde{t}^{1/2} \end{aligned} \quad (25)$$

Thus, we recover the scalings which otherwise were previously derived using equation Eq. (9). Note that if we do not assume the quasi-two-dimensionality for Eq. (22) and instead used $B_n l_{in} l_{jn} \sim \text{const.}$, we would have obtained very different scalings.

In the helical case, instead of Eq. (22), the more important topological constraint is derived from magnetic helicity. Thus, for each structure, we consider

$$B_n^2 l_{in} \sim \text{const.} \quad (26)$$

Here, then we have $B_{n+1} = 2^{-1/6} B_n = 2^{-n/6} B_0$. This will affect the the scaling of S ,

$$S_{n+1} = \frac{B_{n+1} l_{in+1}}{\eta} = \frac{2^{-1/6} B_n 2^{1/3} l_{in}}{\eta} = 2^{1/6} S_n \quad (27)$$

Consequently, instead of Eq. (24), we obtain,

$$\tau_{recn+1} = S_{n+1}^{1/2} \tau_{A_{n+1}} = 2^{7/12} \tau_{A_n} = 2^{7n/12} \tau_0 \quad (28)$$

Note that for calculating τ_{rec} in both cases, we use the 2D Sweet-Parker model. We can then, as before, eliminate n to obtain time dependence of various quantities,

$$\begin{aligned} B &= B_0 \tilde{t}^{-2/7}, & l_1 &= l_{10} \tilde{t}^{4/7} \\ l_2 &= l_{20} \tilde{t}^{4/7}, & l_3 &= l_{30} \tilde{t}^{4/7} \end{aligned} \quad (29)$$

Thus, we recover the scalings observed in our simulations, which are also consistent with the Kolmogorov-type calculation.

6. SOLUTIONS BASED ON SELF-SIMILARITY

Another approach to recovering the scaling laws for decaying turbulence involves leveraging the self-similarity property of the MHD equations, as initially proposed by Olesen (1997). However, the self-similarity scaling suggested by Olesen (1997) resulted in all the physics being determined by the initial MHD spectrum k^α . This limitation was identified by Brandenburg & Kahniashvili (2017), who proposed an improved form for the self-similarity scaling. Such a spectrum is given by,

$$E(k, t) = \xi(t)^{-\beta} \phi(k\xi(t)) \quad (30)$$

where $\xi(\kappa)$ is a universal function, ξ is similar to L_{int} and β governs the envelope traced by the evolving peak wavenumber. Writing down the power law exponents as,

$$p = -\frac{d \ln E_M}{d \ln t}, \quad q = \frac{d \ln L_{int}}{d \ln t}, \quad (31)$$

we obtain,

$$p = (\beta + 1)q. \quad (32)$$

From the above Eq. (32), we can infer the β given the conserved quantity. For example, in the case of magnetic helicity, we have $E_M L_{int} \sim \text{const.}$, which leads to $p = -q$ and, thus, the corresponding $\beta = 0$. However, we need another constraint to recover the exponents p and q themselves.

Traditionally, the scaling solutions assume the inherent timescale in the problem is given by $t_{decay} = L_{int} / \sqrt{E_M}$ or the Alfvénic timescale. For such a relationship, we have

$1 = q + p/2$. However, in the magnetically dominated decaying turbulence, the reconnection timescale becomes important. And then we obtain instead $t_{\text{decay}} = S^{1/2} L_{\text{int}} / \sqrt{E_M}$ which leads to,

$$1 = \frac{1}{4}(6q + p). \quad (33)$$

Now, with Eqs. (32) and (33), we can recover the power law exponents. For the case of fully helical turbulence with $\beta = 0$, we obtain $p = 4/7$ and $q = 4/7$ as before in Eq. (30). In the nonhelical case, $\beta = 1$ for anastrophy conservation. With $\beta = 1$, we recover $p = 1$ and $q = 1/2$ as before in Eq. (26).

7. DISCUSSIONS

DYNAMICAL TIMESCALE IS THE RECONNECTION TIMESCALE. This is best seen in the strict 2D case, where one can explicitly track magnetic islands merging via reconnection. In 3D, it is hard to track reconnecting structures. However BZL21 showed not only curve-collapse in 3D runs with reconnection timescale taken into account, they found a match in 2D and 3D scalings, which we continue to find in helical case as well in this paper. Further, BZL21 study of shell-to-shell energy transfer functions was also consistent with a reconnection-driven system. These results, along with that in Hosking & Schekochihin (2021), seem to rule out Alfvén timescale as the relaxation/decay timescale. However, many other studies continue to regard Alfvén timescale as the decay timescale and thus obtain scaling exponents for magnetic energy that are different but very close to that obtained for reconnection timescale such as $-10/9$ and $-2/3$ for nonhelical and helical cases respectively (as compared to -1 and $-4/7$) (Zhou et al. 2022; Brandenburg 2023; Brandenburg et al. 2023). Another concern is whether many of these studies, which run high-resolution simulations at all, resolve reconnection physics (i.e. current sheet widths).

NECESSITY OF HIGH LUNDQUIST NUMBER AND ITS CONNECTION TO QUASI-TWO-DIMENSIONALITY The simulation results of inverse transfer in nonhelical MHD decaying turbulence posed a puzzle upon their emergence, given the absence of magnetic helicity in this system (Zrake 2014; Brandenburg et al. 2015). Notably, this is a high magnetic Reynolds number or high S (available only at a higher resolution) result, which explains its non-detection in many of the earlier simulations of nonhelical MHD decaying turbulence (Christensson et al. 2001). Thus, a comprehensive understanding of this system should duly consider this important factor. At low S or in a low-resolution simulation, the timescales of operation for microscopic diffusion can get sufficiently short such that any effect of local anisotropy can be rendered ineffective. However, a more significant issue arises when the occurrence of magnetic reconnection is impeded at sites of large current density due to non-negligible diffusion (aided by turbulence). One may inquire about the implications for systems that are not nonhelical. Similar considerations should be taken into account in that scenario as well. Indeed, we observe a steeper decay in lower resolution simulations, which does not necessarily align with the theoretical calculation of $E_M \sim t^{-4/7}$. Thus, whether nonhelical or helical, in both cases, the system at large resolution and high Reynolds numbers tends to be more quasi-two-dimensional. Consequently, it is not surprising when the relevant reconnection time-scale corresponds to a 2D model, i.e., Sweet-Parker reconnection.

A UNIQUELY MHD RESULT This quasi-two-dimensionalization leads to exact same decay laws in both 2D and 3D, which is a uniquely MHD result. Indeed, in hydrodynamics, the 2D and 3D decay laws are different, with different conserved quantities at play. Such a 2D-3D similarity is not to be expected in hydrodynamics unless there is an agent for bringing about quasi-two-dimensionalization, which in the MHD case is naturally manifested by large magnetic field strength (even if the fields are of turbulent nature and reside at smaller scales). In hydrodynamic turbulence, such an agent could be strong rotation, and then the relevant conserved quantities will change back to that relevant in 2D as expected (Yakhot & Pelz 1987).

LOCAL MEAN FIELDS We attribute the quasi-two-dimensionalization to the presence of non-zero local mean magnetic fields. In the standard theories for steady-state magnetically dominated MHD turbulence (either weak or strong), a mean-field is required as the explicit source for anisotropy. The dynamics, then, are described along the mean field separately from across it. Depending on whether the turbulence is weak or strong, connections are made between the dynamics perpendicular and parallel to the mean field (Tobias et al. 2011). In our system, there is no apriori global mean field (or uniform field), however, we postulate that as the strong random fields reconnect, a net local mean field can arise to influence the dynamics locally. This concept aligns with the conventional understanding in standard MHD turbulence theories that, ultimately, the local mean field is important (despite the presence of a uniform mean field) (Cho & Vishniac 2000). However, in this study, we have refrained from directly calculating the local mean fields. The reason is that it is unclear what the scale size for local mean field's region of influence needs to be for it to render the reconnection quasi-2D.

3D RECONNECTION Studies on 3D reconnection are sparse. Most studies either discuss various kinds of manifestations of reconnection sites or arising current instabilities (for e.g. kink instability (Pontin 2011; Landi et al. 2008; Oishi et al. 2015)). While it is well known that a guide field or mean-field renders the ensuing reconnection in the system effectively 2D. Another manifestation of guide field reconnection is when two flux tubes interact at an angle (Linton et al. 2001). However, a complete and systematic characterization of such systems is required for understanding within a larger context of turbulent systems.

PRANDTL NUMBER DEPENDENCE Magnetic reconnection has been shown to be less efficient at higher magnetic Prandtl number $P_M = \nu/\eta$ (Comisso et al. 2015). The associated reconnection timescale is shown to increase with P_M , $\tau_{\text{rec}} \propto (1 + P_M)^{1/2}$. While this has been used to propose that the early universe magnetic fields retain significant amplitude to explain the fields observed in cosmic voids (Hosking & Schekochihin 2023), it is not clear that such a relation should continue to hold at large values of P_M . Some studies suggest that inverse transfer itself gets inefficient with increasing P_M (Armua et al. 2023; Reppin & Banerjee 2017).

ANISOTROPY MEASUREMENT Previous studies that have measured anisotropy have used structure function calculation, taking into account the local mean field in the calculation (Cho & Vishniac 2000). However, given the uncertainty in the required coherence scale for the mean field, we are unable to

use similar techniques. Instead, we use Minkowski functionals to calculate the characteristic length scales of the magnetic field structures. All the three length scales l_1 , l_2 and l_3 we obtain from this analysis are very different, leading to non-zero significant planarity and filamentarity. While the difference between l_1 and l_2 or l_3 can be attributed to local mean-field, that between l_2 and l_3 could be due cross helicity considerations and dynamic alignment (Boldyrev et al. 2009). We have not studied these in this work and leave it for a future investigation.

ISSUE OF GAUGE Already, magnetic helicity is a tricky topological quantity to deal with depending on the nature of the system under study, and there are many issues to consider in its calculation. Depending on the boundary conditions and other ingredients like stratification, large-scale shear, etc, there can be magnetic helicity fluxes which can change the conservation properties dramatically. Then there is the issue related to gauge, which relates to the meaning and interpretation of the results in a system with nontrivial (which are less academic and more realistic) boundaries. But as long as one is in a periodic system, even though local helicity fluxes maybe present due to some inhomogeneities, results can be considered to be robust for the total magnetic helicity.

Similar considerations can be extended to the quantity of vector-potential squared. This quantity is physically connected to the concept of flux-freezing. In 2D, magnetic flux conservation is directly related to the invariance of anastrophy or vector-potential squared. In our decaying nonhelical MHD turbulence case, anastrophy is particularly useful given that the system displays quasi-two-dimensionalization. In the absence of mean magnetic helicity, this quantity displays slower decay time scales compared to magnetic energy and this is fairly nontrivial as, in the case of non-zero magnetic helicity, anastrophy tends to increase with time. In other contexts related to condensates in Yang-Mills theories, the minimization of this quantity w.r.t the topology of the magnetic field, is associated with a gauge condition which is invariant. This is used as a probe of phase transition (Gubarev et al. 2001). Thus, we find that understanding the 3D system with anastrophy is not unjustified on the grounds of gauge arguments as then those would equally apply to a more commonly used 3D quantity like magnetic helicity density.

3D HIERARCHICAL MERGER MODELS In our Quasi-2D Hierarchical Merger (Q2DHM) model, we posit that due to quasi-two-dimensionalization, the magnetic flux conservation constraint is for the in-plane magnetic field (w.r.t reconnection). This is consistent with the requirement of vector-potential squared or anastrophy conservation we discussed above. As mentioned previously, our model is not compatible with that presented in Zhou et al. (2020) as our first constraint of mass conservation leads to Eq. (21), which is not the case in theirs. Further, they draw constraints from strong MHD turbulence of critical balance. The nature of turbulence in this system is not yet fully understood due to the lack of probes on the nature of the local mean fields. However, as mentioned in BZL21, the slope of k^{-2} in the magnetic spectrum is more compatible with that of weak turbulence.

8. CONCLUSIONS

In a previous paper, we had shown that magnetic reconnection is important in decaying nonhelical MHD turbulence. In this work, we showed that the same is true of decaying fully helical MHD turbulence as well. Total magnetic helicity, a conserved quantity in the limit of high Lundquist numbers, is used to constrain the evolution of the helical case. We found that the predicted theoretical power law decay exponent pans out in both 2.5D and 3D simulations. We critically analyzed two possibilities of ideal invariants that could constrain evolution in the nonhelical case, (i) anastrophy or vector potential squared (which is ideally conserved in 2D or 2.5D), $\langle A^2 \rangle$ (ii) the integral based on helicity fluctuations, I_H (which is undefined in strict 2D). We showed that $\langle A^2 \rangle$ has a lower decay rate as compared to I_H or the magnetic energy $\langle B^2 \rangle/2$. Next, we argued that the assumption of the nonhelical system being a composite of fully helical structures of opposite polarities (where the fully nonhelical part decays away on fast timescales) is not valid. We provided evidence for this with (i) a histogram of the cosine angle between vector potential and magnetic field in Fig. 10, where the concentration at and around ± 1 is low, and (ii) we showed that the ration of $E_M^2 k_p^{-5}/I_H \gg 1$. Our final contention was that the same nonhelical behaviour is also observed in strict 2D case, where I_H is basically undefined.

Next, we investigated the possibility of quasi-two-dimensionalization, which can explain the similarity seen in power law decay exponents between 2D (or 2.5D) and 3D cases. To this end, we performed a Minkowski functional analysis for the *reconnecting* magnetic fields. We found that both helical and nonhelical fields have a planarity $P \sim 0.1-0.2$ and filamentarity $F \sim 0.2-0.3$, indicating the existence of local anisotropy. Also, we showed that the fit to power law evolution curves of the characteristic scales, l_1 , l_2 and l_3 displays exponents that are close to the theoretically expected values of 0.5 and 0.57 in nonhelical and helical cases respectively.

We provided a Quasi-2D Hierarchical Merger (Q2DHM) model based on mass conservation and either magnetic flux conservation (in the nonhelical case) or helicity conservation (in the helical case). In this model, we recover the observed scalings only when we consider (i) a 2D manifestation of flux-freezing consistent with vector-potential squared conservation in the plane of reconnection, (ii) and Sweet-Parker model (a 2D model) for reconnection.

ACKNOWLEDGEMENTS

SD, CA and PB are thankful to Prof. Kandaswamy Subramanian for his insightful comments and discussions. We are thankful also to the reviewers for their challenging reports which resulted in further strengthening of our results. SD expresses gratitude to ICTS for hosting her in the Long Term Visiting Students Program. CA thanks Vinay Kumar and Rajarshi Chattopadhyay for their valuable help and discussions. We acknowledge project RTI4001 of the Dept. of Atomic Energy, Govt. of India. SD acknowledges support from the US Dept. of Energy (grant number DE-SC0018266). The simulations were performed on the ICTS HPC cluster *Contra*.

REFERENCES

- Armua A., Berera A., Calderón-Figueroa J., 2023, *Physical Review E*, 107, 055206
 Batchelor G. K., Taylor G. I., 1949, *Proceedings of the Royal Society of London. Series A. Mathematical and Physical Sciences*, 195, 513
 Berera A., Linkmann M., 2014, *Physical Review E*, 90, 041003
 Bhat P., Subramanian K., 2013, *Monthly Notices of the Royal Astronomical Society*, 429, 2469

- Bhat P., Blackman E. G., Subramanian K., 2014, *Monthly Notices of the Royal Astronomical Society*, 438, 2954
- Bhat P., Ebrahimi F., Blackman E. G., Subramanian K., 2017, *Monthly Notices of the Royal Astronomical Society*, 472, 2569
- Bhat P., Zhou M., Loureiro N. F., 2021, *Monthly Notices of the Royal Astronomical Society*, 501, 3074
- Blandford R., Yuan Y., Hoshino M., Sironi L., 2017, *Space Science Reviews*, 207, 291
- Boldyrev S., Mason J., Cattaneo F., 2009, *The Astrophysical Journal*, 699, L39
- Brandenburg A., 2023, *Journal of Plasma Physics*, 89, 175890101
- Brandenburg A., Kahniashvili T., 2017, *Physical Review Letters*, 118, 055102
- Brandenburg A., Kahniashvili T., Tevzadze A. G., 2015, *Physical Review Letters*, 114, 075001
- Brandenburg A., Sharma R., Vachaspati T., 2023, *Journal of Plasma Physics*, 89, 905890606
- Cho J., Vishniac E. T., 2000, *The Astrophysical Journal*, 539, 273
- Christensson M., Hindmarsh M., Brandenburg A., 2001, *Physical Review E*, 64, 056405
- Comisso L., Grasso D., Waelbroeck F. L., 2015, *Physics of Plasmas*, 22, 042109
- Daughton W., Roytershteyn V., Karimabadi H., Yin L., Albright B. J., Bergen B., Bowers K. J., 2011, *Nature Physics*, 7, 539
- Gubarev F. V., Stodolsky L., Zakharov V. I., 2001, *Physical Review Letters*, 86, 2220
- Hesse M., Cassak P. A., 2020, *Journal of Geophysical Research: Space Physics*, 125, e2018JA025935
- Hosking D. N., Schekochihin A. A., 2021, *Physical Review X*, 11, 041005
- Hosking D. N., Schekochihin A. A., 2023, *Nature Communications*, 14, 7523
- Kolmogorov A. N., 1941, *Akademiia Nauk SSSR Doklady*, 32, 16
- Landau L. D., Lifshitz E. M., 1975, *The classical theory of fields*
- Landi S., Londrillo P., Velli M., Bettarini L., 2008, *Physics of Plasmas*, 15, 012302
- Lesieur M., Ossia S., 2000, *Journal of Turbulence*, 1, 007
- Lewiner T., Lopes H., Vieira A. W., Tavares G., 2003, *Journal of Graphics Tools*, 8, 1–15
- Linton M. G., Dahlburg R. B., Antiochos S. K., 2001, *The Astrophysical Journal*, 553, 905
- Lorensen W. E., Cline H. E., 1987, *ACM SIGGRAPH Computer Graphics*, 21, 163–169
- Matthaeus W. H., Montgomery D., 1980, *Annals of the New York Academy of Sciences*, 357, 203
- McKinney J. C., Uzdensky D. A., 2012, *Monthly Notices of the Royal Astronomical Society*, 419, 573
- McPherron R. L., 1979, *Reviews of Geophysics*, 17, 657
- Mecke K. R., Buchert T., Wagner H., 1994, *Astronomy and Astrophysics*, 288, 697
- Mininni P. D., Pouquet A., 2013, *Physical Review E*, 87, 033002
- Moffatt H. K., Kida S., Ohkitani K., 1994, *Journal of Fluid Mechanics*, 259, 241–264
- Narayan R., Igumenshchev I. V., Abramowicz M. A., 2003, *Publications of the Astronomical Society of Japan*, 55, L69
- Neronov A., Vovk I., 2010, *Science*, 328, 73
- Oishi J. S., Low M.-M. M., Collins D. C., Tamura M., 2015, *The Astrophysical Journal Letters*, 806, L12
- Olesen P., 1997, *Physics Letters B*, 398, 321
- Parker E. N., 1983, *The Astrophysical Journal*, 264, 635
- Peebles P. J. E., 1980, *The large-scale structure of the universe*
- Pevtsov A. A., Fisher G. H., Acton L. W., Longcope D. W., Johns-Krull C. M., Kankelborg C. C., Metcalf T. R., 2003, *The Astrophysical Journal*, 598, 1387
- Pontin D. I., 2011, *Advances in Space Research*, 47, 1508
- Pontin D. I., Wilmot-Smith A. L., Hornig G., Galsgaard K., 2011, *Astronomy & Astrophysics*, 525, A57
- Porth O., Komissarov S. S., Keppens R., 2014, *Monthly Notices of the Royal Astronomical Society*, 438, 278
- Pouquet A., Frisch U., Léorat J., 1976, *Journal of Fluid Mechanics*, 77, 321–354
- Priest E., 2016, in Gonzalez W., Parker E., eds, *Astrophysics and Space Science Library, Magnetic Reconnection: Concepts and Applications*. Springer International Publishing, Cham, pp 101–142, doi:10.1007/978-3-319-26432-5_3, https://doi.org/10.1007/978-3-319-26432-5_3
- Rappazzo A. F., Velli M., Einaudi G., Dahlburg R. B., 2008, *The Astrophysical Journal*, 677, 1348
- Reppin J., Banerjee R., 2017, *Physical Review E*, 96, 053105
- Ruan W., Xia C., Keppens R., 2020, *The Astrophysical Journal*, 896, 97
- Sahni V., Sathyaprakash B. S., Shandarin S. F., 1998, *The Astrophysical Journal*, 495, L5
- Seta A., Bushby P. J., Shukurov A., Wood T. S., 2020, *Physical Review Fluids*, 5, 043702
- Sheth J. V., Sahni V., Shandarin S. F., Sathyaprakash B. S., 2003, *Monthly Notices of the Royal Astronomical Society*, 343, 22–46
- Shukurov A., Subramanian K., 2021, *Astrophysical Magnetic Fields: From Galaxies to the Early Universe*. Cambridge Astrophysics, Cambridge University Press, Cambridge, doi:10.1017/9781139046657, https://www.cambridge.org/core/books/astrophysical-magnetic-fields/231CE7B2753A87CEB4BFA55AE04412D1
- Subramanian K., 2016, *Reports on Progress in Physics*, 79, 076901
- Subramanian K., Shukurov A., Haugen N. E. L., 2006, *Monthly Notices of the Royal Astronomical Society*, 366, 1437
- Taylor J. B., 1986, *Reviews of Modern Physics*, 58, 741
- Ting A. C., Matthaeus W. H., Montgomery D., 1986, *The Physics of Fluids*, 29, 3261
- Tobias S. M., Cattaneo F., Boldyrev S., 2011, *MHD Dynamos and Turbulence*, doi:10.48550/arXiv.1103.3138, http://arxiv.org/abs/1103.3138
- Wiegand A., Buchert T., Ostermann M., 2014, *Monthly Notices of the Royal Astronomical Society*, 443, 241
- Wilkin S. L., Barenghi C. F., Shukurov A., 2007, *Physical Review Letters*, 99, 134501
- Yakhot V., Pelz R., 1987, *The Physics of Fluids*, 30, 1272
- Zhdankin V., Boldyrev S., Perez J. C., Tobias S. M., 2014, *The Astrophysical Journal*, 795, 127
- Zhou M., Bhat P., Loureiro N. F., Uzdensky D. A., 2019, *Physical Review Research*, 1, 012004
- Zhou M., Loureiro N. F., Uzdensky D. A., 2020, *Journal of Plasma Physics*, 86, 535860401
- Zhou H., Sharma R., Brandenburg A., 2022, *Journal of Plasma Physics*, 88, 905880602
- Zrake J., 2014, *The Astrophysical Journal*, 794, L26
- Zrake J., 2016, *The Astrophysical Journal*, 823, 39
- Zrake J., Arons J., 2017, *The Astrophysical Journal*, 847, 57

1. Extract isosurfaces from 3D volumetric data

2. Calculate geometric quantities of these isosurfaces

B.1. Iso-surface extraction using marching cubes algorithm

We use the *marching cubes* algorithm to obtain isosurfaces from the data cube. The input data is a scalar function f on a 3D cubic grid. The algorithm samples through each unit cube, hence the name. The algorithm starts by comparing the value of f at each grid point to the user-provided isosurface value. Then, with the help of a pre-defined look-up table, triangles are placed inside a unit cube, thus constituting a triangulation of the surface. The initial algorithm for the look-up table by Lorensen & Cline (1987) had face and internal ambiguities and was later modified by Lewiner et al. (2003) to

APPENDIX

A. TIME EVOLUTION AND MAGNETIC POWER SPECTRA

The complete evolution of rms values of helical magnetic field, magnetic field and velocity fields with time from helical decaying turbulence at different values of S in 2.5D and 3D are shown in Fig. 20.

B. ALGORITHM FOR CALCULATING MINKOWSKI FUNCTIONALS

In section 3.2.4, we have argued that local anisotropy in a 3D turbulent MHD system can render it quasi-two-dimensional. To characterize this local anisotropy, we analyze the shape of magnetic field isosurfaces. The required algorithm must perform the following tasks,

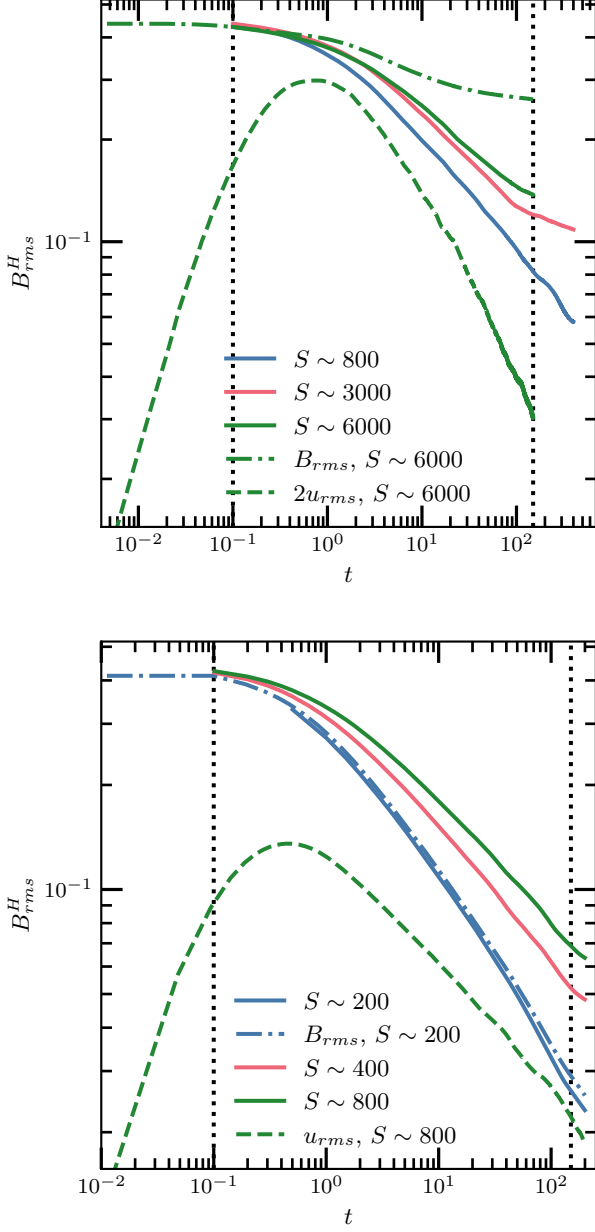


FIG. 20.—: Evolution curves of B_{rms}^H (solid), B_{rms} (dash dot-dotted) and u_{rms} (dashed) with time from fully helical 2.5D (3D) runs on upper panel (lower panel) with different values of S . The black dotted vertical lines denote the time range plotted in Figs. 1 and 2 of Section 3.

create a triangulated surface that is topologically consistent. For our work, we use a Python implementation of the [Lewiner et al. \(2003\)](#) algorithm as in `skimage.measure.marching_cubes` module.

B.2. Quantifying geometric surfaces using Minkowski Functionals

The *marching cubes* algorithm provides us with the position vector for vertices of the triangles and the gradient direction at each vertex of individual triangles in the order of the flow of the algorithm. To calculate Minkowski Functionals of the triangulated isosurfaces, we closely follow [Sheth et al. \(2003\)](#).

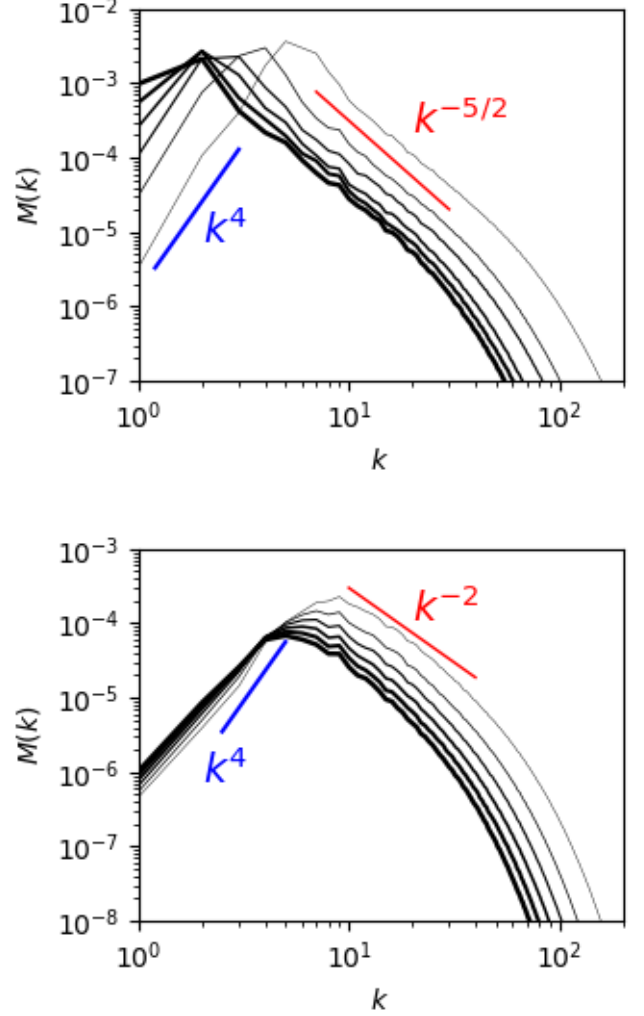


FIG. 21.—: Top panel: Magnetic power spectrum $M(k)$ for 3D helical 1024^3 run with $S \sim 800$ at different time snapshots ($t = 10, 25, 40, 55, 70$) with the thickest at the latest time $t = 85$. Bottom panel: Magnetic power spectrum $M(k)$ for 3D nonhelical 1024^3 run with $S \sim 800$ at different time snapshots ($t = 10, 14, 17, 20, 23$) with the thickest at the latest time $t = 26$.

To separate different connected isosurfaces, we identify the triangles that share an edge with a given triangle.

On a triangulated isosurface, two triangles can share a common edge. Hence, on a connected isosurface, each triangle has three other triangles with which it shares its edges. All the triangles can be viewed together as an undirected graph. Each node of the graph is a triangle. The three edges that come out of a node connect to the three nodes corresponding to the three triangles that share a common edge with the former. Firstly, we construct a sparse matrix indicating triangles that share common edges. Then, we use a graph algorithm implemented in `scipy.cs_graph.connected_components` to identify individual connected structures. To avoid inconsistencies, we impose a lower threshold on the number of triangles making up the isosurfaces. If the number of triangles is less than 10, we reject those isosurfaces.

We restrict to a particular connected structure and obtain the

geometric quantities leading to MFs as follows:

SURFACE AREA The sum of the areas of individual triangles gives the surface area. Using the position vectors for vertices, we calculate the vectors along the edges of the triangles. The area of individual triangles is calculated by taking the absolute value of the cross product of the vectors along any two edges.

VOLUME To calculate the volume, consider one particular triangle on the surface. It subtends a cone at the grid's origin $(0, 0, 0)$. The volume of the triangular cone is,

$$V_i = \frac{1}{3} A_i (\mathbf{P}_c \cdot \hat{\mathbf{n}}), \quad (\text{B1})$$

where A is the area of the base triangle, $\hat{\mathbf{n}}$ is its normal, and \mathbf{P}_c is the position vector of the centroid. The height of the cone is given by $\mathbf{P}_c \cdot \hat{\mathbf{n}}$. Now, consider two triangles 1 and 2 on the 'opposite' sides of the surface as in Fig. 22. The triangle 1's height is 'negative' since the centroid and normal form an obtuse angle. Hence, the volume is 'negative'. However, in the case of triangle 2, the volume is 'positive'. It cancels out the negative contribution from triangle 1, thereby giving us only the volume inside the closed surface. Note that diagonally opposite triangles do not necessarily cancel each other's contribution exactly. We expect that the calculated value converges to the actual value in the limit of a large number of triangles for a given surface. While we described the calculation of the volume subtended at the grid's origin, in practice, we use the centroid of the given structure. However, the above analysis goes through as is.

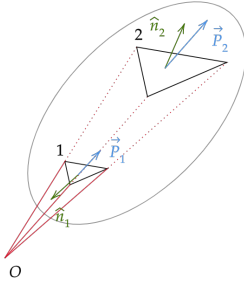


FIG. 22.—: Calculation of volume by summing contributions due to individual tetrahedra formed by the triangles and the origin

INTEGRATED MEAN CURVATURE (IMC) The triangulated surface is curved only at the edges of the triangles and not on the faces. To calculate the curvature at the edges, we fit a cylinder of radius r between two adjoining triangles as shown in Fig. 23. The tangents at the point of contact of the two triangles (i and j) with the cylinder form an angle ϕ_{ij} . The area of this curved surface is $\phi_{ij} l_{ij}$, where l_{ij} is the length of the common edge. The principal curvatures of this cylindrical surface is $\kappa_1 = \frac{1}{r}$ and $\kappa_2 = 0$. The two triangles can be oriented caved in(out), contributing negatively(positively) to the IMC. We quantify the orientation ϵ by calculating the angle between the normal to one of the triangles and the line joining the centroids of the triangles, θ_{ij} (please see Table 2). Hence,

the integrated mean curvature of a structure is,

$$\begin{aligned} C &= \frac{1}{6\pi} \iint (\kappa_1 + \kappa_2) dS = \frac{\epsilon}{6\pi r} \iint dS \\ &= \sum \frac{\epsilon}{6\pi r} r l_{ij} \phi_{ij} = \sum \frac{\epsilon l_{ij} \phi_{ij}}{6\pi}. \quad (\text{B2}) \end{aligned}$$

Orientation	θ_{ij}	ϵ
Convex	$> \frac{\pi}{2}$	+1
Concave	$< \frac{\pi}{2}$	-1
Flat	$\frac{\pi}{2}$	0

TABLE 2

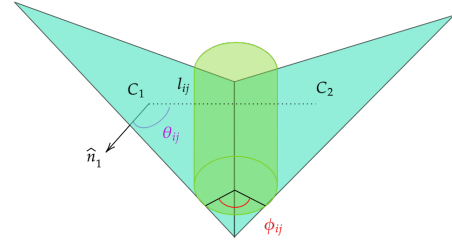


FIG. 23.—: Contribution to IMC from an edge. A cylinder of radius r is fit between the triangular surfaces. They subtend an angle ϕ_{ij} , and the common edge has length l_{ij} . The normal at triangle 1 and the line joining the triangles 1, 2 subtend an angle θ_{ij} .

GAUSS CURVATURE The Gauss curvature is calculated using the Gauss-Bonnet theorem, which relates it to the Euler characteristic. The Gauss-Bonnet theorem states that

$$\int_M K dS = 2\pi \chi(M), \quad (\text{B3})$$

where $K = \kappa_1 \kappa_2$. In particular, the above theorem holds also for polyhedral surfaces. Hence, given a triangulation of the surface and thereby the number of vertices V , edges E , and faces F , the Euler characteristic is,

$$\chi = V - E + F = V - \frac{3}{2}F + F = V - \frac{F}{2}. \quad (\text{B4})$$

We have used the fact that each triangle has three edges, two triangles share each edge, and thus, $E = \frac{3}{2}F$.

C. IDENTIFICATION OF SITES OF RECONNECTION AND NEARBY MAGNETIC FIELD ISO-SURFACES

We compute the MFs for $|\mathbf{B}|$ and $|\mathbf{J}|$ fields. While computing MFs for structures throughout the 1024^3 domain is computationally demanding, it is not necessary as we mainly want to focus on magnetic fields near reconnection sites. We identify reconnection sites or grid points which have a large current density value. We quantify this by taking a cutoff value for the current density, $0.7 * |\mathbf{J}|_{\max}$. This threshold was chosen to obtain a sufficient number of structures that ensure reliable statistics.

To avoid repetition of processing grid points pertaining to the same current sheet, we isolate a set by the following method. We first apply the threshold (mentioned above) to

$|\mathbf{J}|$ to obtain a set of grid-points. Individual clusters of points *belonging* to a current sheet are identified by:

- (a) Ensuring furthest points in a given cluster are separated at the maximum by $0.5 L_{int}$ to prevent the inclusion of neighbouring current sheets,
- (b) Ensuring that each cluster is separated from another by at least $1.5 L_{int}$.

In this manner, we also avoid double counting of magnetic field isosurfaces. We choose the point with the maximum value among each cluster as the representative point for that cluster. We define the *current sheet* in this cluster to be the isosurface with isovalue $0.5 * |\mathbf{J}|_{\max, \text{cluster}}$. Henceforth, we focus our attention on individual current sheets. For a given current sheet, we restrict our domain size to be L_{int} about its representative point. We do so in order to identify magnetic field isosurfaces that are in proximity to the current sheet.

To do the MF analysis, we adopt the following scheme to determine, first, the isovalues for $|\mathbf{B}|$. We want to map out the radial profile of $|\mathbf{B}|$ around the current sheet. Ideally, an infinite number of rays with all possible orientations are needed, but we use 50 rays with random orientations to get an optimal balance between computational cost and sufficiency. We parametrize the rays from $[-0.5, 0.5] L_{int}$ with 100 points. We calculate the $|\mathbf{B}|$ value along the rays by linear interpolation. The maximum and the minimum values of the $|\mathbf{B}|$ along each ray nearest to the representative point are obtained. Among these extrema, the largest maximum and the smallest minimum value of $|\mathbf{B}|$ are calculated and labelled as $|\mathbf{B}|_{\max}$ and $|\mathbf{B}|_{\min}$ respectively. Finally, we choose the isovalues for the magnetic field in the following manner,

$$|\mathbf{B}|_{\max} - \frac{i}{5} \times \left(\frac{|\mathbf{B}|_{\max} - |\mathbf{B}|_{\min}}{4} \right) \quad \forall i \in 1, 2, 3, 4, 5. \quad (\text{C1})$$

This approach of selecting isovalues is to prevent the isosurfaces from being either minuscule compared to the grid separation or volume-filling. Once the magnetic isosurfaces are identified in this way, MFs can be calculated. Since there can be multiple magnetic field isosurfaces, we want to consider the isosurface closest to the current sheet. So, we calculate the distance between the current sheet and the $|\mathbf{B}|$ field isosurfaces⁶ and choose the isosurface with the smallest distance to the current sheet.

A particular simulation can be considered one realization from an ensemble of turbulent configurations. The reconnection sites that we obtain form a sample of all possible realizations. Having obtained the MFs of $|\mathbf{B}|$ and $|\mathbf{J}|$ isosurfaces, we calculate the sample average and standard error⁷ of

the isosurfaces across all isovalues considered. We then plot the evolution of sample averages with standard errors as error bars.

D. MF ANALYSIS OF CURRENT SHEETS

D.1. Evolution of P and F for current sheets

Here, we display the evolution of the Minkowski Functionals for the current sheets in Fig. 24 and in Fig. 25 for the helical and nonhelical cases respectively. We already noted in Fig. 19 that the current isosurfaces in both the helical and nonhelical cases are sheet-like. We plot the evolution of l_1 , l_2 and l_3 for the current sheets and observe that they increase with time. This behaviour of the current sheet is consistent with the fact that the system relaxes to larger and larger scales. We then plot the evolution of P and F . The P and F of the current sheets are almost constant with time for both helical ($P \sim t^{0.15 \pm 0.03}$, $F \sim t^{0.02 \pm 0.04}$) and nonhelical ($P \sim t^{0.01 \pm 0.03}$, $F \sim t^{-0.11 \pm 0.04}$) cases. We also report the linear fits for the length scales l in the plot.

E. RESULTS FROM FORCED HYDRODYNAMIC TURBULENCE

We simulated forced hydrodynamic turbulence with a grid size of 512^3 , average forcing wavenumber $k_f \approx 1.5$, and zero initial velocity field. When the turbulence is fully developed (we confirm the $k^{-5/3}$ spectrum), we perform the morphological analysis using MF. At time $t = 80$, we look at the saturation of the velocity field and confirm that turbulence has fully developed in the system. In 3D hydrodynamic turbulence, the high vorticity isosurfaces are present as tubular structures (Moffatt et al. 1994). Hence, we expect structures with isovalues higher than ω_{rms} at a particular time to be statistically filamentary (large F). A preliminary visual confirmation is seen in Fig. 26. We calculate MF of ω at an isovalue of $5\omega_{rms}$. Initially, we plot the histogram of planarity and filamentarity in Fig. 27. We plot the mean volume in each bin to understand where the structures of various sizes (volume) contribute. On sequentially removing surfaces with volumes less than a certain fraction of the total mean volume, the peak of the histogram shifts to higher values for filamentarity and lower values for planarity. Hence, larger structures are predominantly filamentarity with an almost circular cross-section (with normal along the long axis). Hence, the system is statistically tube-like.

This paper was built using the Open Journal of Astrophysics L^AT_EX template. The OJA is a journal which provides fast and easy peer review for new papers in the astro-ph section of the arXiv, making the reviewing process simpler for authors and referees alike. Learn more at <http://astro.theoj.org>.

⁶ The distance between two sets, $d(C, D) = \min d(x_C, x_D)$

⁷ It is the standard deviation divided by the square root of the sample size.

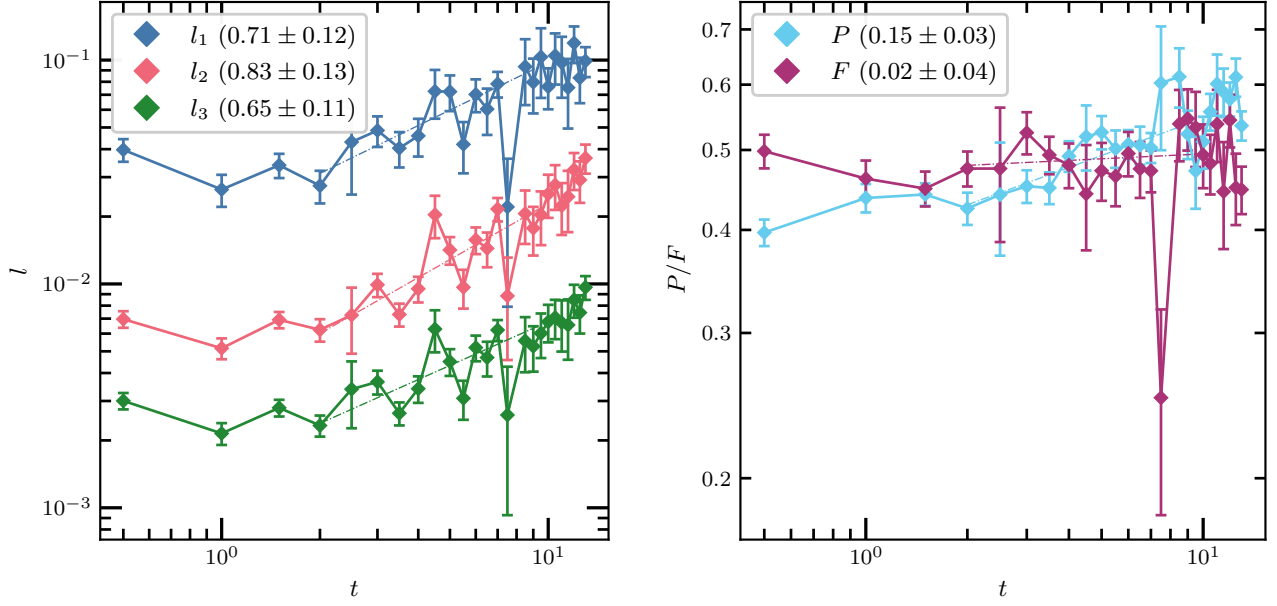


FIG. 24.— **Helical:** The time evolution of length scales of *current sheet* isosurfaces is shown in the left panel. The different dashed curves are the least square fit. Time evolution of P and F in the early stages of the decay (when the B_{rms} curve behaviour is close to the theoretical prediction of $t^{-2/7}$) is shown in the right panel.

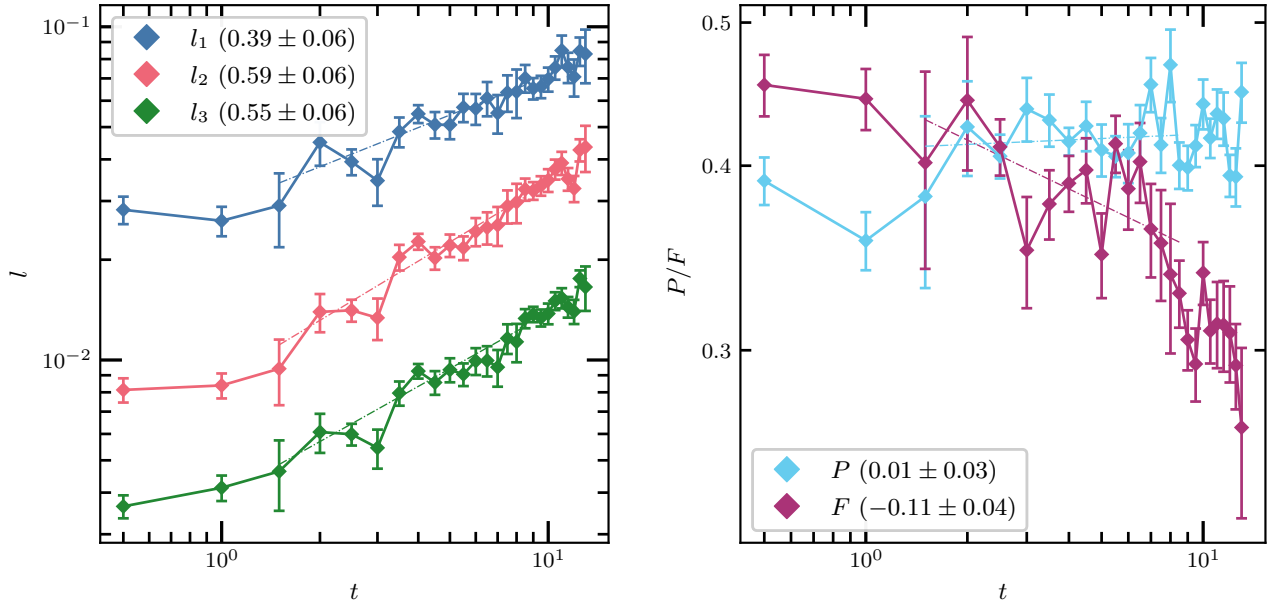


FIG. 25.— **Nonhelical:** The time evolution of length scales of *current sheet* isosurfaces is shown in the left panel. The different dashed curves are the least square fit. Time evolution of P and F in the early stages of the decay (when the B_{rms} curve behaviour is close to the theoretical prediction of $t^{-1/2}$) is shown in the right panel.

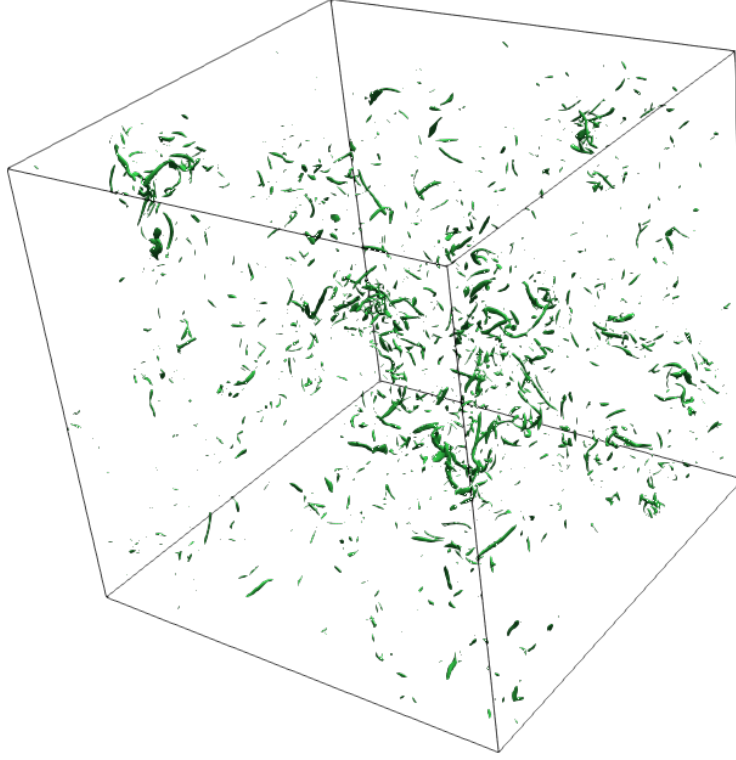


FIG. 26.—: Isosurfaces of vorticity fields at isovalue $5\omega_{\text{rms}}$ of a forced hydrodynamics 512^3 simulations at $t = 80$. From the figure, it is clear that the structures are akin to elongated tubes.

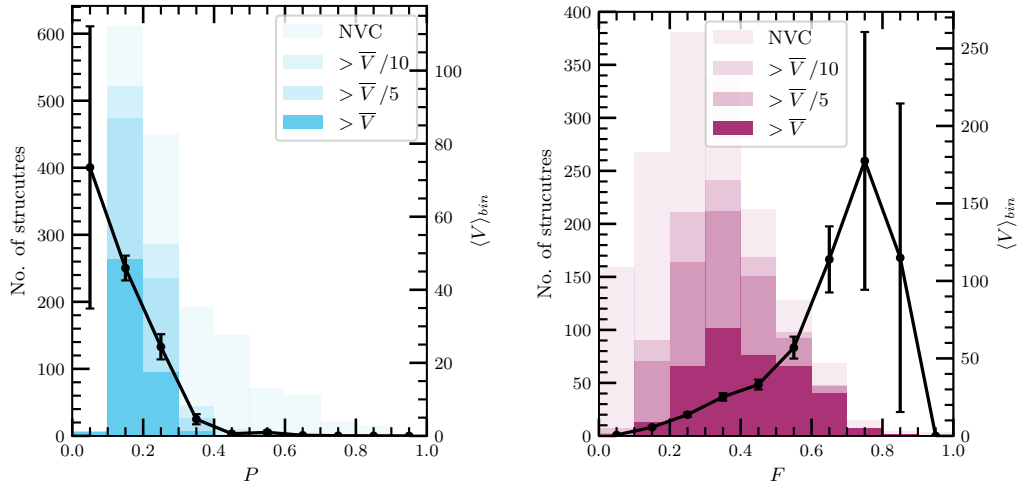


FIG. 27.—: Histogram for planarity (left panel) and filamentarity (right panel) of all the vorticity structures at isovalue $5\omega_{\text{rms}}$ in the forced hydrodynamics 512^3 simulation at $t = 80$. Also shown in the black circles is the average volume in each bin. NVC stands for no-volume-cutoff. The darker shades represent statistics for structures considered above a certain volume threshold denoted by \bar{V}/n and $n = 1, 5$ or 10 . The tendency of large structures to have smaller planarity and larger filamentarity is clear from the graph. The same conclusion can also be reached by progressively considering structures with larger and larger volumes, as we have shown in this plot.